Biaxial Material Design Method for the Reduced Aperture Waveguide Model

A thesis submitted in partial fulfillment
of the requirements for the degree of
Master of Science in Engineering

by

Jason M. Brand
B.S.E.E., Wright State University, 2013

2014
Wright State University

Wright State University
Graduate School

December 11, 2014

I HEREBY RECOMMEND THAT THE THESIS PREPARED UNDER MY SUPERVISION BY Jason M. Brand ENTITLED Biaxial Material Design Method for the Reduced Aperture Waveguide Model BE ACCEPTED IN PARTIAL FULFILLMENT OF THE REQUIREMENTS FOR THE DEGREE OF Master of Science in Engineering.

Michael A. Saville, Ph.D., P.E.
Thesis Director

Brian D Rigling, Ph.D.
Chair, Department of Electrical Engineering
College of Engineering and Computer Science

Committee on
Final Examination

Michael A.Saville, Ph.D., P.E.

Doug Petkie, Ph.D.

Yan Zhuang, Ph.D.

Robert E.W. Fyffe, Ph.D
Vice President for Research and
Dean of the Graduate School

ABSTRACT

Brand, Jason. M.S.Egr., Department of Electrical Engineering, Wright State University, 2014. *Biaxial Material Design Method for the Reduced Aperture Waveguide Model.*

The design and characterization of metamaterials has emerged as a field of great interest in electromagnetics in recent years. The characterization has been accomplished primarily by means of fabrication, measurement, and parameter estimation. Previous work by Knisely and Havrilla [8] has shown that biaxial anisotropy can be created by machining air vias uniaxially into a homogeneous, isotropic material. This research project proposes a design method for manufactured biaxial materials. Full wave modeling and simulation is used for samples with varying via size, separation and pose to obtain the scattering parameters S_{11} and S_{21}. To compare the simulated S-parameters to theoretical S-parameters of different dielectric values solved by mode matching, a cost function was created. The cost function is minimized using a constrained non-linear least squares optimization technique. When the global minimum of the cost function is found the material parameter for the values that optimized the function are estimated to be the values of the simulated material.

Contents

List of Figures

List of Tables

Acknowledgment

I would like to take this opportunity to extend my thanks to my adviser Dr. Michael A. Saville for his patience, guidance, and support through this process. Without which I never would have made it through. Thank you for this opportunity.

To my Signal and Sensor Exploitation Lab mates, both past and present, thank you for your support and being available as a sounding board when needed. The friendship and knowledge we have shared will remain with me forever.

To the office staff of the Electrical Engineering office whos continued support helped me through this process.

I would like to thank my committee members for being available on such short notice. The time you have taken to help with this process is appreciated.

Dedicated to

To my family. Without whose support, love, and extreme patience this would have been an impossible journey. I know that this will fall short of expressing my true gratitude but Thank You.

Introduction

1.1 Metamaterials

The term metamaterials has been ambiguous since it was first introduced. For the scope of this research project, the term will be used as defined by Dr. Smith at the Duke Meta Group. Dr. Smith defines metamaterial as ”any material with properties not found in nature [1]”.

One example of a manufactured metamaterial was show by Dr. Nathan Kundtz [2]. In his dissertation, it is proposed that to insert a metamaterial slab in the path of a propagating electric field causes the path of the field to change in a manner consistent with the properties of the guiding structure. Figure 1.1 shows the result of this theory.

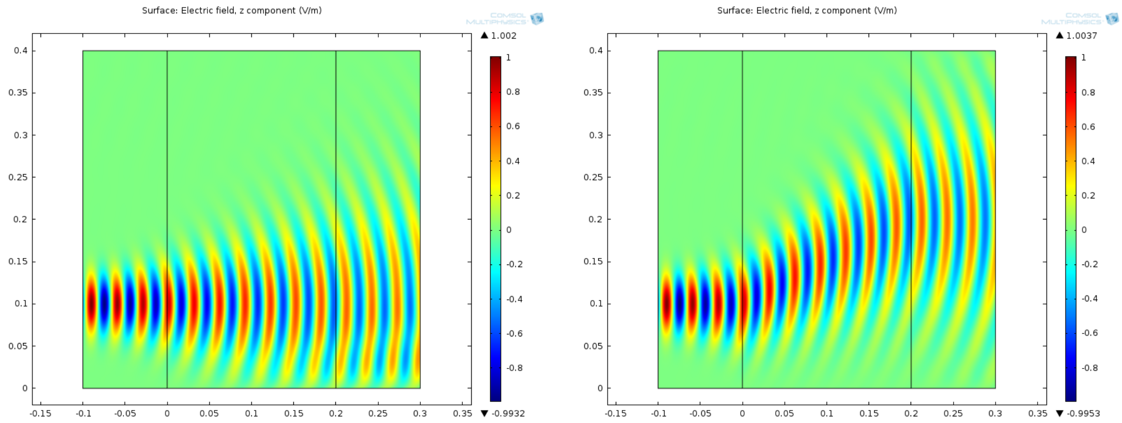

Figure 1.1: (Left) The electric field propagating in free space. (Right) The resulting propagation path of the electric field when a metamaterial has been inserted from 0 to 0.2 [2]

A second example for metamaterials was proposed by Dr. Popa [3] who showed that the metamaterial can be designed using conformal mapping. In [3], the metamaterial analysis and design will allow one array of antennas to produce the same far field radiation pattern as another array (Fig 1.2).

A well-known example of metamaterial application and design was given by Dr. Nathan Pendry [4]. Pendry's design causes the electromagnetic waves to propagate around an occupied region of space as it were void. Hence, the name invisibility cloak. The results of which are shown in Fig. 1.3. One complication that arises in these examples is that the electric permittivity and magnetic permeability $\bar{\bar{\epsilon}}$ and $\bar{\bar{\mu}}$ are strongly anisotropic, lossy, and inhomogeneous.

Figure 1.4 shows the metamaterial design that Dr. Pendry used to create the electromagnetic cloaking device. The cloak consists of concentric circles of individual resonant structures where the layering results in the desired anisotropic and non-homogeneous properties. While this design is one possible way to create materials, this research project will be focused on a material design process that allows for the use of weakly anisotropic and inhomogeneous materials. The approach is based on the method developed by Havrilla et al [9]. The proposed method allows for the creation of anisotropic material from bulk

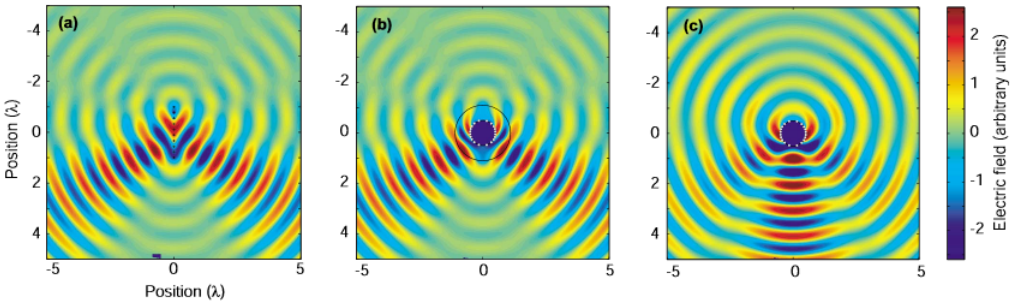

Figure 1.2: (Left) Radiation pattern of a linear array of radiators. (Right) Radiation pattern of a circular array of radiators around a Perfect Magnetic Conductor. (Center) Radiation pattern of a circular array of radiators around a Perfect Magnetic conductor surrounded by a metamaterial. Metamaterial causes the radiation pattern to mimic that of the linear array.

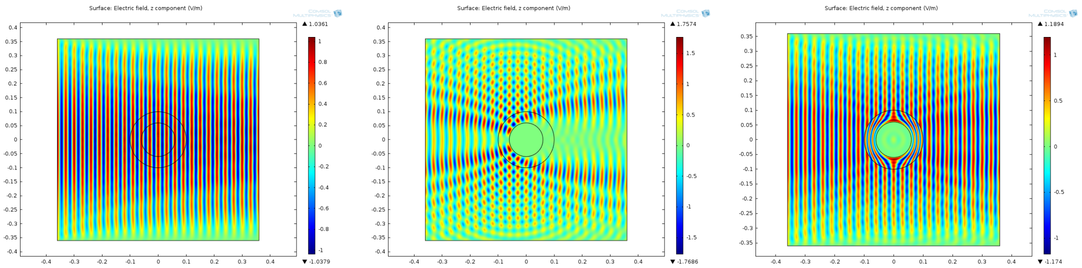

Figure 1.3: (Left) Electric field as it propagates in free space. (Center)Show the propagation pattern of the field with a circular Perfect Electric Conducting object inserted. (Right) Propagation of the field with the PEC object surrounded by a meta material designed to provide the cloaking properties.

material.

In Ref. [9], a bulk simple (homogeneous, isotropic, and linear) material is machined into a cube that perfectly fits a cubic sample holder. Anisotropic behavior is achieved by drilling vias or ducts along one axis the sample [5]. The example in Fig.1.5 shows vias were created in a square lattice while Fig.1.6 shows a 3D perspective of the vias which are created uniaxially in the bulk material and extend the entire length of the test sample.

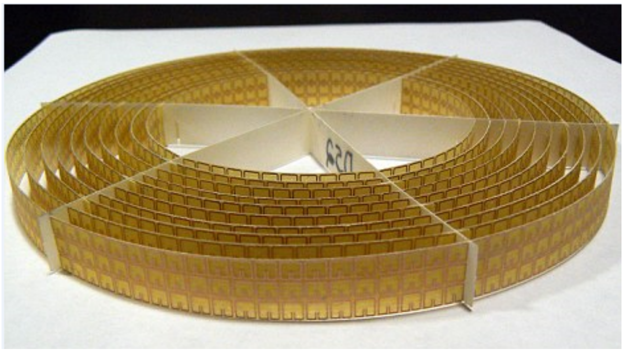

Figure 1.4: The meta material cloak designed by Dr. Pendry. [4]

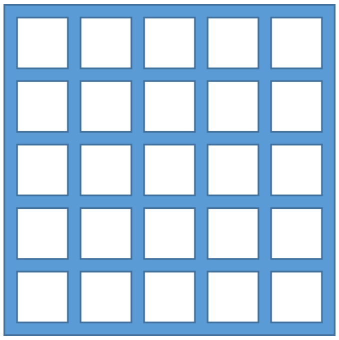

Figure 1.5: Example of a metamaterial containing 25 air vias in a 5 by 5 lattice. The shaded region representing the bulk material and the clear region represents the air vias.

By creating these vias in the bulk simple material the electromagnetic properties will be adjusted allowing for the materials to become inhomogeneous or biaxial in nature. One should note however that the material's dielectric properties are bound by the inherent properties of the bulk material. Anisotropic material properties will be discussed in 2.1.1.

1.2 Challenges

The primary challenge in the creation of metamaterials is to find a design system that allows the creator to predict what the properties of the material will be before it is manufactured as well as how changing parameters in the material design will affect the electromagnetic

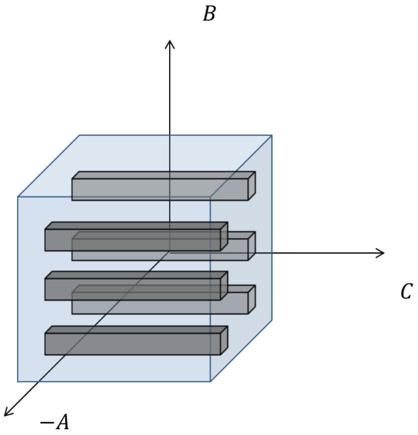

Figure 1.6: Oblique view of a uniaxially machined material.

properties. Another issue is that depending on the outcome of the material properties a frequency selective material can be inadvertently created due to a resonance behavior at certain frequencies. There are also production constraints that can be placed on the material; for example, size constraints of the vias, separation between the vias, or the bulk material dielectric properties.

1.3 Research Hypothesis

This research project proposes a design method for the uniaxially machined biaxial material. It is believed that the simple periodic lattice can be designed to achieve specific values of permittivity and permeability. However, this work will focus on the method which uses full-wave electromagnetic modeling and simulation and non-linear optimization of the via size, dimensions, and pose.

1.4 Outline

The outline of this thesis is as follows. Chapter 2 will present a review of pertinent electromagnetic theory that will be of use throughout the paper. The theory will be followed by an overview of biaxial material properties and how they affect Maxwell's equations. Then it will explain the three methods that were used to perform, verify and extract the data from the necessary simulations. Chapter 3 describes the proposed method. Chapter 4 presents the results and discusses how density of air-to-dielectric and shape of the vias affects the permittivity and permeability. Finally, Chapter 5 summarizes the work and proposes future research goals pertaining to parameter extraction from simulated metamaterials.

Background

2.1 Maxwell's Equations

The study of electromagnetic fields is at its core the study of the interaction of charges and the materials around them. When the charges are at rest the fields they create are quite simple to represent even with algebra. When the charges are put into motion the defining formulas become much more complicated as they progress into a series of partial differential equations. The first of Maxwell's equations which is used to determine the electric field is Farday's Law which states

$$\nabla \times \vec{E} = -\vec{M}_i - \frac{\partial \vec{B}}{\partial t}. \tag{2.1}$$

The magnetic field is given by the second equation know as Ampere's Law stating that

$$\nabla \times \vec{H} = \vec{J}_i + \frac{\partial \vec{D}}{\partial t}. \tag{2.2}$$

For simple media (2.1) and (2.2) are used to derive the wave equation [6]

$$\nabla^2 \vec{E} - \mu\sigma \frac{\partial \vec{E}}{\partial t} - \mu\epsilon \frac{\partial^2 \vec{E}}{\partial t^2} = \nabla \times \vec{M}_i + \mu \frac{\partial \vec{J}_i}{\partial t} \tag{2.3}$$

with $\vec{M}_i$ being any magnetic currents and $\vec{J}_i$ representing electric currents. The solution of (2.3) will show the properties of a wave traveling in a simple media, for example

$$E = E_0 \cos(\beta x + \phi) \tag{2.4}$$

2.1.1 Biaxial Materials

While (2.3) shows how the fields behave inside a simple media, in general a material has more complicated properties: anisotropy, non-homogeneity, dispersiveness, non-linearity. This work focuses on the aniotropic property where the permittivity is

$$\bar{\bar{\epsilon}} = \begin{bmatrix} \epsilon_{xx} & \epsilon_{xy} & \epsilon_{xz} \\ \epsilon_{yx} & \epsilon_{yy} & \epsilon_{yz} \\ \epsilon_{zx} & \epsilon_{zy} & \epsilon_{zz} \end{bmatrix} \tag{2.5}$$

and the permeability is

$$\bar{\bar{\mu}} = \begin{bmatrix} \mu_{xx} & \mu_{xy} & \mu_{xz} \\ \mu_{yx} & \mu_{yy} & \mu_{yz} \\ \mu_{zx} & \mu_{zy} & \mu_{zz} \end{bmatrix}. \tag{2.6}$$

Equations (2.5) and (2.6) are best understood by their constitutive relations

$$\begin{aligned} \vec{D} &= \bar{\bar{\epsilon}}\vec{E} \\ \vec{B} &= \bar{\bar{\mu}}\vec{H} \end{aligned} \tag{2.7}$$

which relate electric and magnetic fluxes to fields.

For example, ϵ_{yx}, ϵ_{yy}, and ϵ_{yz} represents how the flux of the $\hat{y}$ component responds to an arbitrary electric field, i.e. $D_y = \epsilon_{yx}E_x + \epsilon_{yy}E_y + \epsilon_{yz}E_z$. A more in depth look at the vector calculus is presented in [7].

Following a similar procedure as was done for simple media the wave equation for anisotropic and inhomogeneous materials becomes

$$\nabla \times \bar{\bar{\mu}}^{-1} \nabla \times \vec{E} + \sigma \frac{\partial \vec{E}}{\partial t} + \bar{\bar{\epsilon}} \frac{\partial^2 \vec{E}}{\partial t^2} = -\frac{\partial \vec{J}_i}{\partial t} - \nabla \times \bar{\bar{\mu}}^{-1} \vec{M}_i. \tag{2.8}$$

While the simple wave equation (2.4) can be given in a simple form. The anisotropic wave equation (2.8) does not have an easy solution and is generally solved by numerical methods.

2.1.2 Boundary Conditions

Mawell's equations and the wave equations that were derived from them take the form of vector partial differential equations; the solutions provide the field vectors under the constraints that the fields are single-valued and bounded[6]. However, unique solutions are determined from the enforcement of boundary conditions which occur when there is a change of material. An excellent example of electromagnetic boundary conditions is illustrated in the solution of fields propagating in a waveguide[6].

When two materials with different dielectric properties share a boundary the electric field must satisfy

$$\hat{n} \times (\vec{E_2} - \vec{E_1}) = \vec{M_s} \tag{2.9}$$

and the magnetic field must satisfy

$$\hat{n} \times (\vec{M_2} - \vec{M_1}) = \vec{J_s}. \tag{2.10}$$

These relations mean that assuming there are no impressed currents or free charges at the boundary both (2.9) and (2.10) will equal zero; the tangential components of both the electric and magnetic fields will be continuous across the boundary.

The normal components of the fluxes behave in a similar fashion as

$$\hat{n} \cdot (\vec{D}_2 - \vec{D}_1) = \vec{q}_{es} \tag{2.11}$$

and

$$\hat{n} \cdot (\vec{B}_2 - \vec{B}_1) = \vec{q}_{ms}. \tag{2.12}$$

The normal components of the electric and magnetic fields will be discontinuous across the boundary by an amount equal to the the amount of charge that exists on that boundary. However, the normal components of the electric and magnetic fields are discontinuous by the material properties:

$$\begin{aligned} \hat{n} \cdot (\epsilon_2 \vec{E}_2 - \epsilon_1 \vec{E}_1) &= 0 \\ \hat{n} \cdot (\mu_2 \vec{H}_2 - \mu_1 \vec{H}_1) &= 0 \end{aligned} \tag{2.13}$$

or

$$\begin{aligned} \vec{E}_{2n} &= \frac{\epsilon_1}{\epsilon_2} \vec{E}_{1n} \\ \vec{H}_{2n} &= \frac{\mu_1}{\mu_2} \vec{H}_{1n} \end{aligned} \tag{2.14}$$

where E_{2n} and E_{1n} represent the normal components of the electric and magnetic fields. For propagation across a half-space (Fig. 2.1) the normal component will be discontinuous by an amount relative to the ratio of the dielectric properties.

The second boundary condition that is of concern to this research project is that between a PEC boundary and another material because the waveguide test fixture is assumed to have PEC walls. A PEC is a theoretical material in which the resistivity(σ) is considered to be infinite. While a PEC does not exist naturally in nature there are some substances

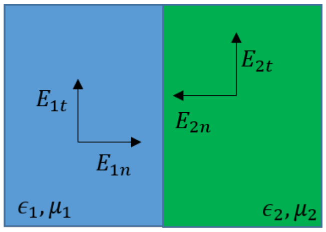

Figure 2.1: An example of the boundary of two unlike materials.

that can be estimated to contain these properties, e.g. silver, copper, and aluminum. As a result of having a negligible resistivity any charges that accumulate on the surface of the material will distribute themselves in such a way to make the field inside it come to zero. By looking at Fig. 2.2, which shows an illustration of the transverse cross-section of a WR90 waveguide, and labeling the fields inside the waveguide as $\vec{E}_2$ and the fields in the PEC region as $\vec{E}_1$ the boundary conditions (2.9) and (2.11) become

$$\begin{aligned} \hat{n} \times \vec{E}_2 &= 0 \\ \hat{n} \cdot \vec{D}_2 &= 0. \end{aligned} \tag{2.15}$$

At the PEC material interface the normal and tangential components of the electric field must be zero. The boundary conditions of the rectangular waveguide shown in Fig. 2.2 results in electric fields inside the guide with form

$$\begin{gathered} \text{TE} : A_{mn} \cos(\beta_x x) \sin(\beta_y y) e^{-j\beta_z z}, \text{TE}^z, \begin{cases} m, n = 0, 1, ..., \infty \\ m = n \neq 0 \end{cases} \\ \text{TM} : B_{mn} \cos(\beta_x x) \cos(\beta_y y) e^{-j\beta_z z}, \text{TM}^z, m, n = 1, 2, ..., \infty \end{gathered} \tag{2.16}$$

where the wave functions $\cos()$ and $\sin()$ represent the standing waves, the exponential represents the propagating wave and the dispersion relation is

$$\beta^2 = \omega^2 \mu \epsilon = \beta_x^2 + \beta_y^2 + \beta_z^2 \tag{2.17}$$

The specific forms of $\beta_x, \beta_y, \beta_z$ depend on the material and cross-sectional shape of the guide.

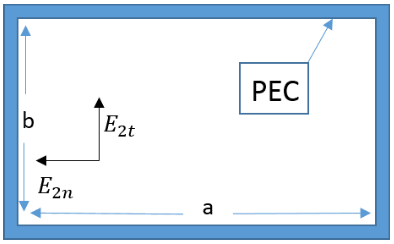

Figure 2.2: An example of PEC waveguide

2.1.3 Mode Matching

Mode matching is a method of analysis for guiding structures that compares the propagating modes in different sections by applying boundary conditions at each junction[5]. As an example, the reduced aperture waveguide test fixture of [9] is analyzed by solving a linear system of equations formed by enforcement of boundary conditions. Figure 2.3 illustrates two different sections of waveguide. When the system is excited from region A, coefficients shown in Fig. 2.3 will result.

Figure 2.4 shows an air filled waveguide ($z < 0, z > d$) with an anisotropic sample contained in the sample holder ($0 < z < d$). A TE_{10} excitation will be used in the left region and due to the symmetry of the guide only TE_{n0} fields will exist throughout [9]. When the wave reaches the sample holder ($z = 0$) there will be a reflection of waves due to a mismatch. Also, geometric discontinuities cause scattered waves at the junctions. The portion of the TE_{n0} waves not reflected back towards the source will continue through the sample region until the point when the sample region meets the right portion of the air filled waveguide ($z = d$) and again a portion will be reflected and a portion transmitted. This behavior causes waves to exist in the sample region that travel in both the $+z$ and $-z$ direction. Finally, the transmitted portion of the wave will continue to travel to the right most air-filled waveguide ($z > d$) without obstruction due to the assumption of a perfectly matched port allowing for the appearance of an infinite waveguide section. By forming a set of linear equations of the TE_{n0} modes in each region, from the boundary conditions, the strength of the modes can be computed using matrix algebra. the process of expanding the fields into a series of TE_{n0} modes and determining the coefficients is mode matching. The exact form of the mode matching model of reduced aperture waveguide is outlined in 2.2.2.

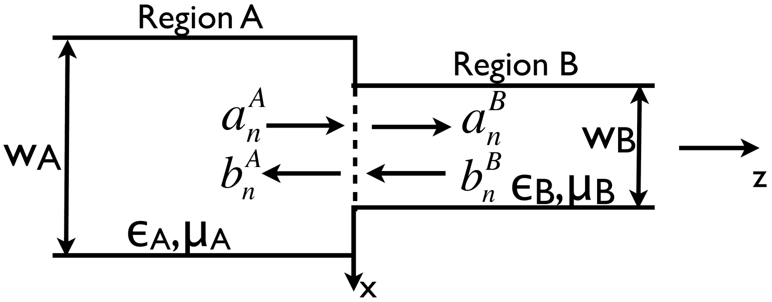

Figure 2.3: Outline of the sections of reduced aperture waveguide used for Mode Matching. Image from [10].

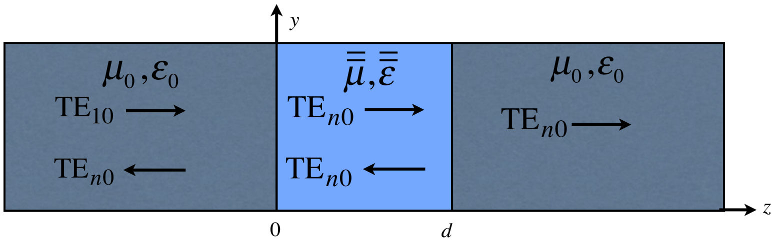

Figure 2.4: Cross sectional view of the reduced aperture sample system. Image from [10].

2.2 Characterization Methods

As metamaterials have gained popularity in recent years so to has the desire to accurately characterize the properties of these materials. Many methods have been developed in the pursuit of this goal such as waveguide measurement systems [13], resonant cavity measurement systems [15], free space methods [14], rectangular to square measurement system [8], and the reduced aperture method [9]. One commonality between all of the methods is that they all require the material to be physically created. Different electromagnetic quantities are measured from which the permittivity and permeability can be estimated. Measurements are also limited. The resonant cavity measurement system is only valid around the frequencies that the cavity resonates. The waveguide measurement system can only be used with uniaxially anisotropic materials for a single sample. In order to extract the biaxial anisotropic properties from Eqs. (2.5) and (2.6) three samples must be created which increases the chance for manufacturing error to effect the properties. The free space method which requires exciting a field with a spot beam on the material requires large sample sizes with regard to the size of the beam to limit fringing. The rectangular-to-square and reduced-aperture systems allow for biaxial parameters to be extracted with a single relatively small sample which provides an advantage over the other measurement methods.

2.2.1 Reduced Aperture Waveguide

The reduced aperture waveguide (RAW) is a system that was introduced by Dr. Crowgey in [9] and illustrated in Fig. 2.5. Dr. Crowgey derived a procedure in which the tensor quantities could be extracted using scattering parameters from a RAW measurement system. Although shown for S-band frequencies, the technique scales with waveguide size. This technique has the advantage in that it only requires a single cubic sample. The utilization of a cubic sample allows for all of the S-parameters required for permittivity and permeability extraction to be accomplished with a set of four measurement configurations.

The test sample is machined and placed in the sample holder and excited by a TE_{10} mode and the S-parameters are measured. This procedure is then repeated with the sample being rotated in various orientations to excite each of the primary axes of the test sample. The parameter extraction process is then accomplished by minimizing the difference between the measured S-parameters and the theoretical S-Parameters that are obtained via the mode matching solution (Section 2.2.2).

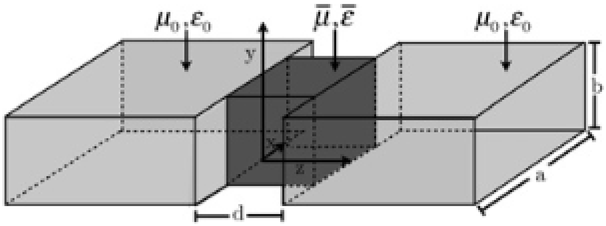

Figure 2.5: A picture of the RAW as shown by Crowgey. Taken from [9].

2.2.2 Reduced Aperture Mode Matching Solution

In the reduced aperture waveguide model [9] shown in Fig. 2.6 an analytical solution was put forth that would allow for the verification of different simulation methods of the testing structure. The chosen analytic solution is a mode matching method which is ideal for this problem as it resembles a layered material problem. the formulation presented in this section closely follows [9]to allow the reader to better understand the material extraction method presented in Section 3.3. To start it would be useful to look at the wave equation for the material inside the sample region (Region B). By placing the material so it is biaxial with respect to the of x, y, z directions and considering a TE_z excitation in the sample region the magnetic field wave function $h_x(x, y)$ satisfies [9]

$$\frac{\mu_x}{\beta^2 - k_0^2\mu_x\epsilon_y}\frac{\partial^2 h_z}{\partial x^2} + \frac{\mu_y}{\beta^2 - k_0^2\mu_y\epsilon_x}\frac{\partial^2 h_z}{\partial y^2} - \mu_z h_z = 0 \tag{2.18}$$

where $k_0 = \omega\sqrt{\mu_0\epsilon_0}$. For TE_z fields, $H(x, y, z) = h_z(x, y)e^{\pm j\beta z}$, and for TE_{10} excitation there will be no y dependency in the wave equation which reduces to

$$\left(\frac{\partial^2}{\partial x^2} + k_c^2\right)h_z(x) = 0 \tag{2.19}$$

The cut off frequency k_c^2 is

$$k_c^2 = \frac{\mu_z}{\mu_x}(k_0^2\mu_x\epsilon_y - \beta^2). \tag{2.20}$$

By solving the differential equation and applying the boundary conditions for a perfect electric conducting wave guide the modal tangential electric field $e^s_{y,n}(x)$ and modal tangential magnetic fields $h^s_{x,n}(x)$ are given as [9]

$$e_{y,n}(x) = \sin\left(k^s_{c,n}\left(x - \frac{w}{2}\right)\right) \tag{2.21}$$

$$h^s_{x,n}(x) = \pm\frac{e^s_{y,n}(x)}{Z^s_n}. \tag{2.22}$$

By accounting for the forward propagating excitation ($A_1^+ e^e_{y,1}(x)e^{-j\beta^e_1 z}$) and the summation of the reflected fields that exist in region A ($\sum_{\substack{n=1 \\ odd}}^{\infty} A_n^- e^e_{y,n}(x)e^{j\beta^e_n z}$) the total field becomes

$$E_y(x, z) = A_1^+ e^e_{y,1}(x)e^{-j\beta^e_1 z} + \sum_{\substack{n=1 \\ odd}}^{\infty} A_n^- e^e_{y,n}(x)e^{j\beta^e_n z}. \tag{2.23}$$

Similarly the total magnetic field can be shown as

$$H_x(x, z) = -\frac{A_1^+ e^e_{y,1}(x)}{Z^e_1}e^{-j\beta^e_1 z} + \sum_{\substack{n=1 \\ odd}}^{\infty} \frac{A_n^- e^e_{y,n}(x)}{Z^e_n}e^{j\beta^e_n z}. \tag{2.24}$$

In the definition of the wave functions $e^{j\omega t}$ time convention is assumed. Hence, $e^{-j\beta z}$

represents a forward propagating wave.

In region B the fields will be an infinite sum of both forward and reverse traveling waves represented as

$$E_y(x,z) = \sum_{\substack{n=1\\odd}}^{\infty}[B_n^+ e^{-j\beta_n^s} + B_n^- e^{j\beta_n^s z}]e^s_{y,n}(x) \tag{2.25}$$

$$H_x(x,z) = \sum_{\substack{n=1\\odd}}^{\infty}\left[\frac{B_n^+}{Z_n^s} e^{-j\beta_n^s} + \frac{B_n^-}{Z_n^s} e^{j\beta_n^s z}\right]e^s_{y,n}(x) \tag{2.26}$$

where the coefficients B_n^+ and B_n^- represent the complex amplitudes. The fields in region C of the model will only contain forward propagating waves due to the perfect match at the end of the waveguide. This regions fields are represented as

$$E_y(x,z) = \sum_{\substack{n=1\\odd}}^{\infty} C_n^+ e^e_{y,n}(x) e^{-j\beta_n^e (z-d)} \tag{2.27}$$

$$H_x(x,z) = \sum_{\substack{n=1\\odd}}^{\infty} \frac{C_n^+}{Z_n^e} e^e_{y,n}(x) e^{-j\beta_n^e (z-d)}. \tag{2.28}$$

Once the equations have been determined there are 4 coefficients that must be determined A^-, B^-, B^+, and C^+. It should be noted that since A^+ represents the excitation field in the waveguide this is known. The 4 unknown coefficients are found by applying the electric and magnetic boundary conditions at the two boundaries $z = 0$ and $z = d$.

At $z = 0$,

$$A_1^+ e^e_{y,1}(x) + \sum_{\substack{n=1\\odd}}^{\infty} A_n^- e^e_{y,n}(x) = \begin{cases} \sum_{\substack{n=1\\odd}}^{\infty}[B_n^+ + B_n^-]e^s_{y,n}(x), & 0 < |x| < \frac{w}{2} \\ 0, & \frac{w}{2} < |x| < \frac{a}{2} \end{cases}$$

(2.29)

represents the total electric field.

The total magnetic field at $z = 0$ becomes

$$\begin{aligned} -A_1^+ \frac{e_{y,1}^e(x)}{Z_1^e} + \sum_{\substack{n=1 \\ odd}}^{\infty} \frac{A_n^- e_{y,n}^e(x)}{Z_1^e} = \\ \sum_{\substack{n=1 \\ odd}}^{\infty} \left[-\frac{B_n^+}{Z_n^s} + \frac{B_n^-}{Z_n^s} \right] e_{y,n}^s(x), 0 < |x| < \frac{w}{2}. \end{aligned} \tag{2.30}$$

The other two equations used to solve for the coefficients are derived by enforcing the boundary conditions at $z = d$. These boundary conditions cause the electric field to be defined as

$$\sum_{\substack{n=1 \\ odd}}^{\infty} C_n^+ e_{y,1}^e(x) = \begin{cases} \sum_{\substack{n=1 \\ odd}}^{\infty} [B_n^+ e^{-j\beta_n^s d} + B_n^- e^{j\beta_n^s d}] e_{y,n}^s(x), & 0 < |x| < \frac{w}{2} \\ 0, & \frac{w}{2} < |x| < \frac{a}{2} \end{cases}. \tag{2.31}$$

By the same approach, the H field at $z > d$ becomes

$$\begin{aligned} -\sum_{\substack{n=1 \\ odd}}^{\infty} \frac{C_n^+}{Z_n^e} e_{y,n}^e(x) = \\ \sum_{\substack{n=1 \\ odd}}^{\infty} \left[-\frac{B_n^+}{Z_n^s} e^{-j\beta_n^s d} + \frac{B_n^-}{Z_n^s} e^{j\beta_n^s d} \right] e_{y,n}^s(x), 0 < |x| < \frac{w}{2}. \end{aligned} \tag{2.32}$$

Equations (2.2.2) to (2.32) can be solved using matrix algebra and the scattering parameters S_{11} and S_{21} can be calculated as

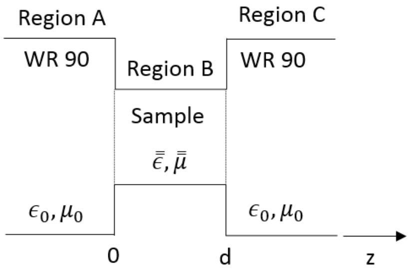

Figure 2.6: A diagram of the reduced aperture waveguide. Region A and C are lengths of WR-90 waveguide. Region B is a square sample region.

$$\begin{aligned} S_{11} &= \frac{A_1^-}{A_1^+} \\ S_{12} &= \frac{C_1^+}{A_1^+}. \end{aligned} \tag{2.33}$$

2.2.3 Parameter Extraction

The parameter extraction introduced in [9] is a straight forward process that involves comparing the theoretical from Section 2.2.2 $S_{21}^{thy}(\epsilon)$ for a given permittivity and the measured S_{21}^{meas} for a sample under test. The unknown quantity ϵ of the physical sample is determined by

$$S_{21}^{thy}(\epsilon) - S_{21}^{meas} = 0 \tag{2.34}$$

In [9], these values are determined using Newton's method.

For the biaxial case, Dr. Crowgey places the the sample in 4 orientations conforming to

$$(A, B, C) \to (x, y, z) \Rightarrow [S_{11,1}^{meas} \; S_{21,1}^{meas}], \tag{2.35}$$

$$(A, B, C) \to (-z, y, x) \Rightarrow [S_{11,2}^{meas} \; S_{21,2}^{meas}], \tag{2.36}$$

$$(A, B, C) \to (y, -x, z) \Rightarrow [S_{11,3}^{meas} \; S_{21,3}^{meas}], \tag{2.37}$$

$$(A, B, C) \rightarrow (z, x, y) \Rightarrow [S_{11,4}^{meas} \; S_{21,4}^{meas}]. \tag{2.38}$$

With the S-Parameters measured from the 4 orientations (2.35) to (2.38) and the relation given in (2.34) all six of the unknown complex material parameters $(\epsilon_A, \epsilon_B, \epsilon_C, \mu_A, \mu_B, \mu_C)$ can be found [9].

The first three values $(\epsilon_B, \mu_A, \mu_C)$ can be solved finding the solution to

$$S_{11,n}^{thy}(\epsilon_B, \mu_A, \mu_C) - S_{11,n}^{meas} = 0, \; n = 1 \tag{2.39}$$

$$S_{21,n}^{thy}(\epsilon_B, \mu_A, \mu_C) - S_{21,n}^{meas} = 0, \; n = 1, 2. \tag{2.40}$$

Next using the parameters from (2.37) ϵ_A and μ_B can be determined by using a Newton's method on

$$S_{11,3}^{thy}(\epsilon_A, \mu_B) - S_{11,3}^{meas} = 0, \tag{2.41}$$

$$S_{21,3}^{thy}(\epsilon_A, \mu_B) - S_{21,3}^{meas} = 0, \tag{2.42}$$

The final unknown parameter (ϵ_C) is found using

$$S_{21,4}^{thy}(\epsilon_C) - S_{21,4}^{meas} = 0. \tag{2.43}$$

While this method does require a fourth measurement to be taken Dr. Crowgey has found that the reduction of unknowns in each step is advantageous.

A second method of parameter extraction was introduced by Dr. Nicolson in [16]. Dr Nicolson presented a measurement method in which a disk of material with thickness d is placed in an air-filled coaxial waveguide Fig. 2.7. When excited an electromagnetic wave travels through the air-filled region with characteristic impedance Z_0 until reaching the disc at A where the characteristic impedance becomes [16]

$$Z = \sqrt{\frac{\mu_r}{\epsilon_r}} Z_0 \tag{2.44}$$

If d were extended to be infinite in length the reflection coefficient is shown to be

$$\Gamma = \frac{\sqrt{\frac{\mu_r}{\epsilon_r}} - 1}{\sqrt{\frac{\mu_r}{\epsilon_r}} + 1}. \tag{2.45}$$

By limiting the thickness to a finite value of d the transmission coefficient in the disk becomes

$$z = e^{-j\frac{\omega}{c}\sqrt{\epsilon_r \mu_r} d} \tag{2.46}$$

Using microwave theory the S_{11} and S_{21} of the system can be determined by treating this as a 4 port system, as shown in Fig. 2.7, with

$$\begin{aligned} S_{11} &= \frac{V_A}{V_{inc}} = \frac{(1-z^2)\Gamma}{1-\Gamma^2 z^2} \\ S_{21} &= \frac{V_B}{V_{inc}} = \frac{(1-\Gamma^2)z}{1-\Gamma^2 z^2}. \end{aligned} \tag{2.47}$$

By adding and subtracting S_{11} and S_{21}

$$\begin{aligned} V_1 &= S_{21} + S_{11} \\ V_2 &= S_{21} - S_{11} \end{aligned} \tag{2.48}$$

and if χ is defined as

$$\chi = \frac{1 - V_1 V_2}{V_1 - V_2} \tag{2.49}$$

then the reflection coefficient can be defined as

$$\Gamma = \chi \pm \sqrt{\chi^2 - 1} \tag{2.50}$$

The sign is chosen to ensure $|\Gamma| \leq 1$. Also, z can also be defined in terms of reflection coefficients as

$$z = \frac{V_1 - \Gamma}{1 - V_1\Gamma}. \tag{2.51}$$

Now (2.45) can be use to define c_1 as

$$\frac{\mu_r}{\epsilon_r} = {\frac{1+\Gamma}{1-\Gamma}}^{2} = c_1 \tag{2.52}$$

and (2.46) to define c_2 as

$$\mu_r\epsilon_r = -\{\frac{c}{}ln\frac{1}{z}\}^2 = c_2. \tag{2.53}$$

These two equations can then be used to derive the complex permittivity and permeability as

$$\begin{aligned} \mu_r &= \sqrt{c_1 c_2} \\ \epsilon_r &= \sqrt{\frac{c_2}{c_1}}. \end{aligned} \tag{2.54}$$

For the purpose of this research project the method of extraction introduced in [16] is not practical since it requires a hole in the material for the center conductor to pass through. Due to this project's focus on periodic structures this is less than ideal as the presence of the center conductor would break the periodic nature of the lattice. The center conductor would also have an unwanted effect on the air-to-dielectric ratio.

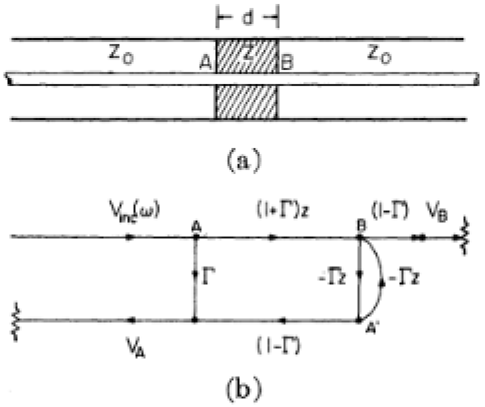

Figure 2.7: Dielectric measurement system using transmission line system. Taken from [16].

2.3 Finite Element Method

The Finite Element Method (FEM) is a mathematical model that is used as an approximation method to solve the boundary-value problem of the partial differential equations proposed by Maxwell's Equations[11]. The FEM involves dividing the solution space into a set of sub wavelength mesh points. The solution is then calculated at these points and interpolated to the areas between them. For the scope of this research project COMSOL Multiphysics®will be used as the FEM solver. FEM is a well-known and standard method used to solve radiation, guided wave and scattering problems for exotic material properties.

Experiment Methodology

The premise of this research project is that by using computational electromagnetics(CEM) methods in lieu of measurements the structure of a metamaterial can be designed to produce desired dielectric properties. Before this can occur, the simulation model must be created and verified. The verification of the CEM model will be completed by comparing the results from the simulated model to the results of the mode matching model with the sample holder being filled with air. Once the CEM model has been built and verified a partial factorial experimental design will be used to study the effects of the size, dimensions, and pose of the vias discussed in Section 3.2. Parameter extraction, i.e., estimation of $\bar{\bar{\epsilon}}, \bar{\bar{\mu}}$ will be accomplished using a non-linear constrained least squares algorithm implemented in MATLAB.

3.1 The Model

Following the reduced aperture waveguide used by Crowgey [9], which was created for operation at S-band, the dimensions are scaled to that of WR-90 waveguide and modeled in COMSOL. This base model (seen in Fig. 3.1) consists of a full wavelength of WR-90 PEC waveguide connected to a reduced aperture cubic sample holder having the same height dimensions as the height of the waveguide. That is then followed by another full wavelength of waveguide Fig.3.1. One wavelength corresponds to the longest wavelength under test (8 GHz or 3.75 cm).

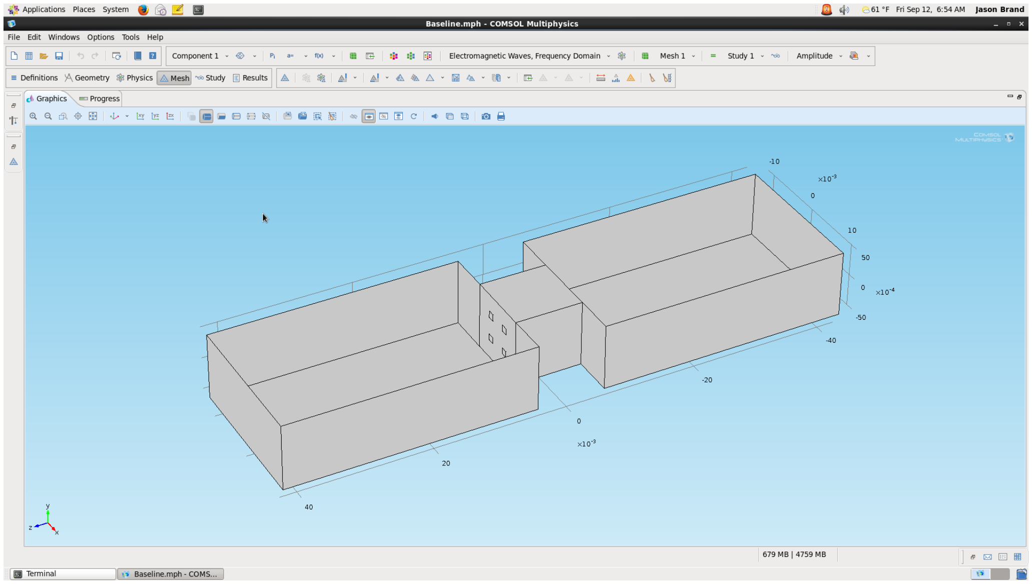

Figure 3.1: Reduced Aperture model with full wavelength of waveguide before and after holder

With the RAW built and modeled in COMSOL the FEM results were obtained for an air-filled sample holder. The S_{11} and S_{21} were then compared to the S-Parameters obtained from the mode matching solution of Section 2.2.2. The error results for S_{11} are shown in Fig. 3.2 and are $O(10^{-3})$ to $O(10^{-2})$.

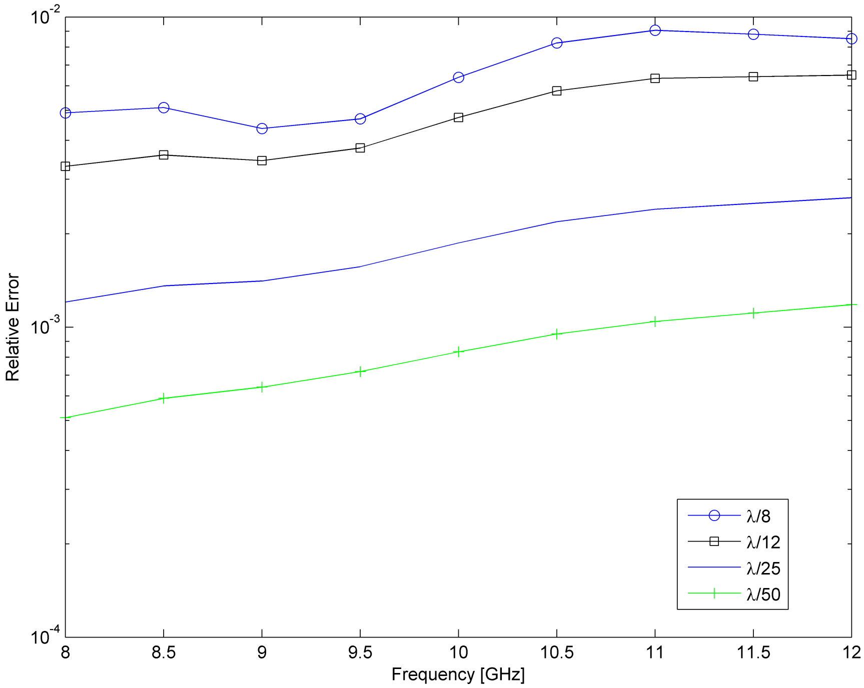

Figure 3.2: Error of S_{11} for a simulated reduced aperture structure with full wavelength of waveguide before and after air filled sample holder compared to numerical solution at variable mesh sizes

Figure 3.3 shows the relative error contained in the S_{21} of the simulation model when compared to the analytic solution. These errors are a bit higher than the S_{11} data ranging from $O(10^{-3})$ to $O(10^{-1.5})$. Due to propagation of the error through the process and the constraints that are placed on the parameter extraction process larger mesh elements $\frac{\lambda}{8}$ and $\frac{\lambda}{12}$ will be avoided in the simulation portion of the project. The reason being that the optimization is sensitive to errors that are on the order of convergence tolerance. This method will compare the values of the experimental data to the mode matching solution. Since the S-parameter error is greater than 10^{-2} and that error propagates through the process it will not be possible to satisfy the tolerance set in the routine.

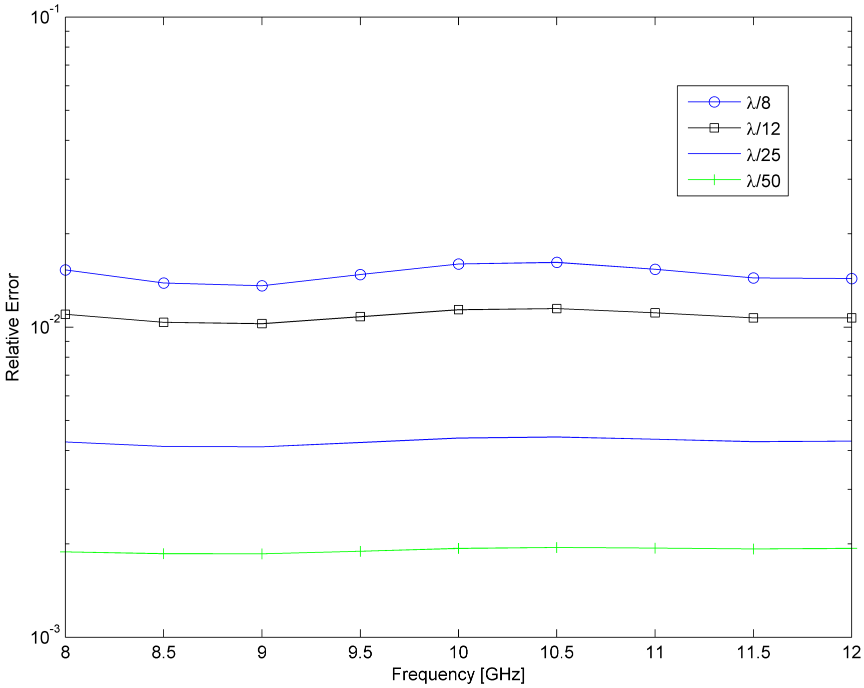

Figure 3.3: Error of S_{21} for a simulated reduced aperture structure with full wavelength of waveguide before and after air filled sample holder compared to numerical solution at variable mesh sizes

With a large number of simulations required to analyze the effects of changing certain design parameters, a reduction of the size of the RAW model was made. This reduction came in the form of shortening the λ-length waveguide sections to $\frac{\lambda}{3}$ (Fig. 3.4). This change could affect the accuracy of the S-Parameters being measured. Higher-order modes are created by scattering off the discontinuities in the guide, but evanesce before reaching the measurement planes. In order to assure that this change in the system would not affect the accuracy of the model a verification was made to examine the error contained in the S-Parameters just as was done with the original model. Figure 3.5 shows the error of the modified system which remains within the acceptable error constraints actually providing a smoother distribution than the original model. Figure 3.6 shows the error in the S_{21} from the modified system which exhibits similar error levels to the original model.

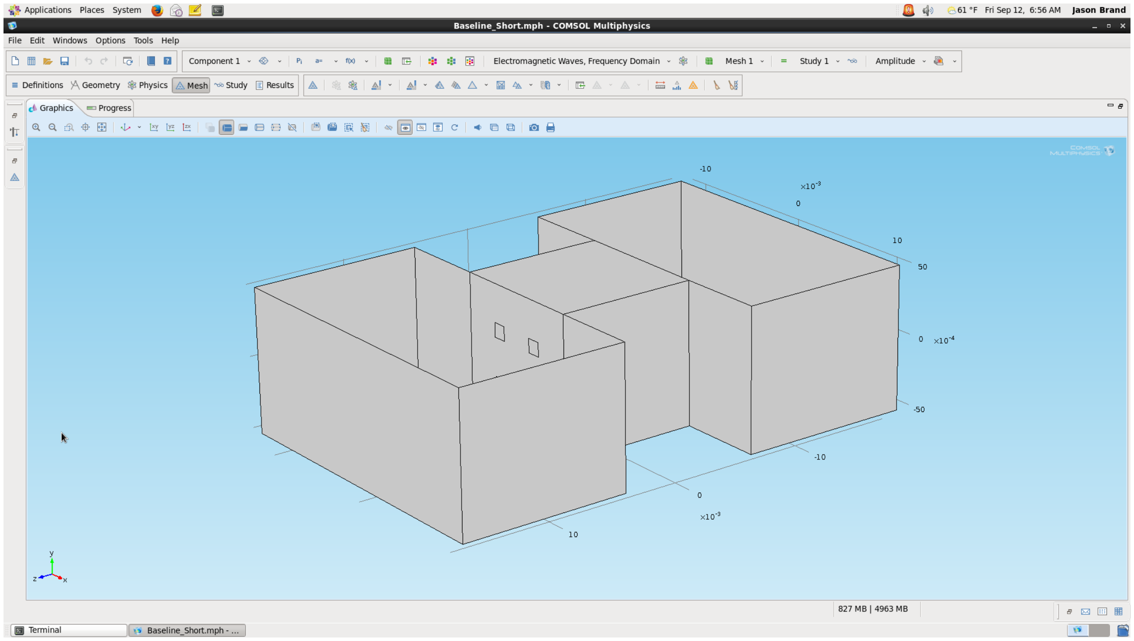

Figure 3.4: Reduced Aperture model with 1/3 wavelength of waveguide before and after holder

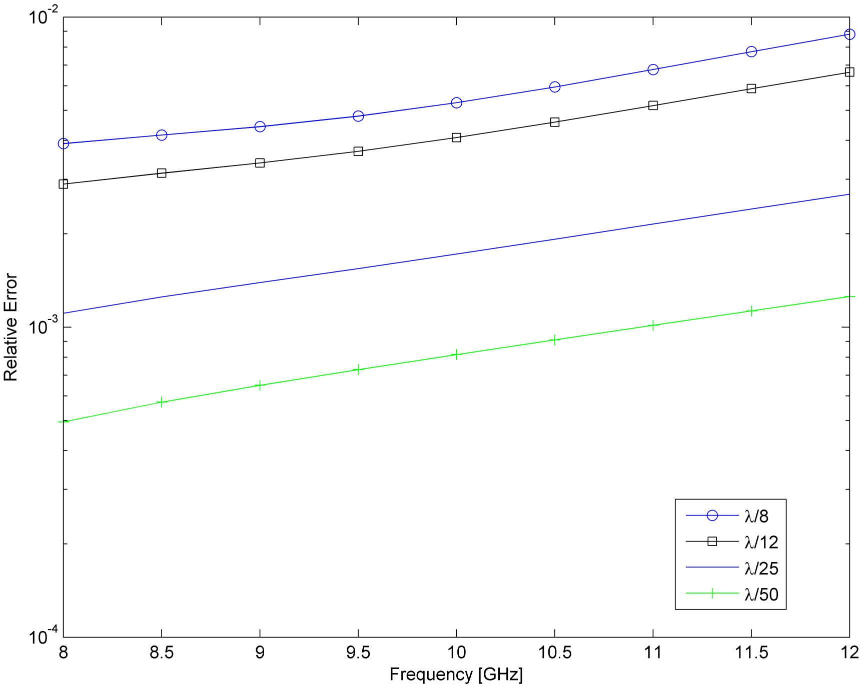

Figure 3.5: Error of S_{11} for a simulated reduced aperture structure with $\frac{\lambda}{3}$ of waveguide before and after air filled sample holder compared to numerical solution at variable mesh sizes

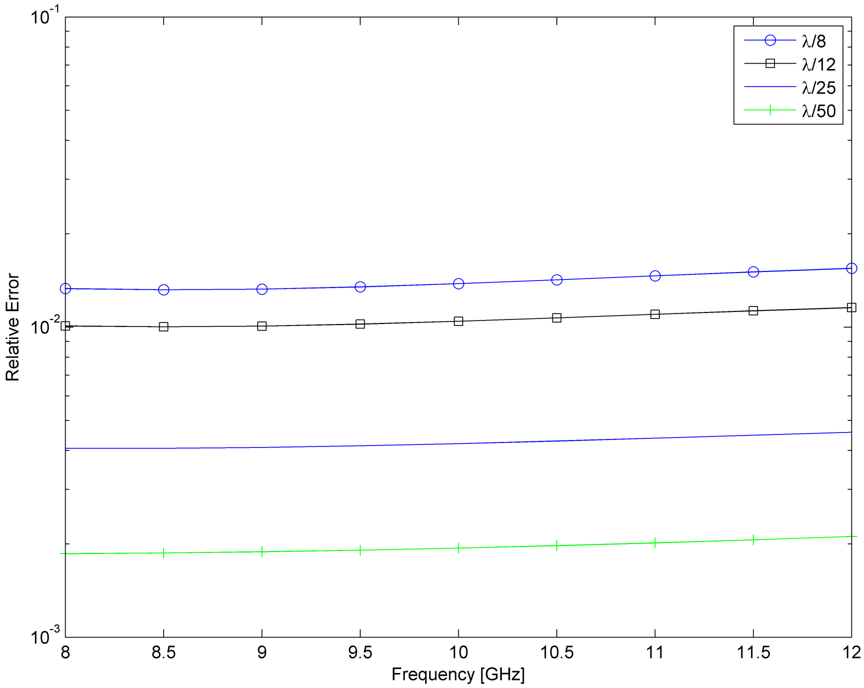

Figure 3.6: Error of S_{21} for a simulated reduced aperture structure with $\frac{\lambda}{3}$ wavelength of waveguide before and after air filled sample holder compared to numerical solution at variable mesh sizes

When comparing the results of the simulation error (shown in Fig. 3.2 to 3.6) it can be seen that by shortening the waveguide we can eliminate 41.61% of the computational volume while maintaining the same error levels.

3.2 Experiment Design

The experiment design used for this research project will consist of a partial factorial method of experiments meaning that certain independent variables (size, separation, pose of vias) in the material under test (MUT) will be altered and simulated using the finite elements method. However, due to limited resources for simulation only a subset of the S-Parameters will be exported and run through a MATLAB parameter extraction process yielding the 6 complex material properties.

The initial test was designed to compare the number of vias, along with the size and separation of the vias. The values explored are shown in Table 3.1 with δ representing the size of the square vias, lattice size representing the number of vias in each dimension of the sample (nxn), and D_x representing the separation between each via. The variable ρ was created as a tool for demonstrating the ratio of base dielectric material to air in the sample and defined as

$$\rho = \frac{\delta_x N_x \delta_y N_y}{XY - \delta_x N_x \delta_y N_y} \tag{3.1}$$

with δ_x representing the size in the x direction of the via, N_x the number of vias in the x direction, δ_y the size of the vias in the y direction, N_y the number of vias in the y direction, and XY representing the area of the sample holder. Since all vias are uniaxial and span the entire depth of the MUT only the ratio on the single face must be found and will accurately represent the entire volume of the sample.

Trial	Via Size $\delta(mm)$	Lattice size (nxn)	Separation Dx(mm)	Ratio of material to air (ρ)
1	1	2	2.72	.040312178
2	1	3	1.79	.095515444
3	1.5	2	2.38667	.09551544
4	1	4	1.232	0.183432387
5	2	2	2.05333	0.183432387
6	1.5	3	1.415	0.244047648
7	1	5	0.86	0.31958847
8	2.5	2	1.72	0.3195885
9	1	6	0.5943	0.5355103
10	1.5	4	0.832	0.5355103
11	2	3	1.04	0.5355
12	3	2	1.387	0.5355
13	1	7	0.395	0.9036322
14	3.5	2	1.0533	0.90363223
15	1.5	5	0.4433	1.19743016
16	2.5	3	0.665	1.19743016
17	2	4	0.432	1.6316
18	4	2	0.72	1.631588
19	1.5	6	0.1657	3.644
20	3	3	0.29	3.6445
21	4.5	2	0.38667	3.644446
22	2	5	.02667	31.00198
23	5	2	.05333	31.00198

Table 3.1: Partial factorial experiment design of via size and separation.

3.3 Parameter Extraction

With the desired sample configurations established, a simulation procedure was created to retrieve the 6 complex S-Parameters that are used in the parameter extraction code. This was accomplished by using a y-directed TE_{10} excitation in the modified RAW test system shown in Fig. 3.4 of Section 3.1 and rotating the sample in the sample holder to excite the sample along the primary axes (shown in Fig. 3.7) in a 4 step measurement process.

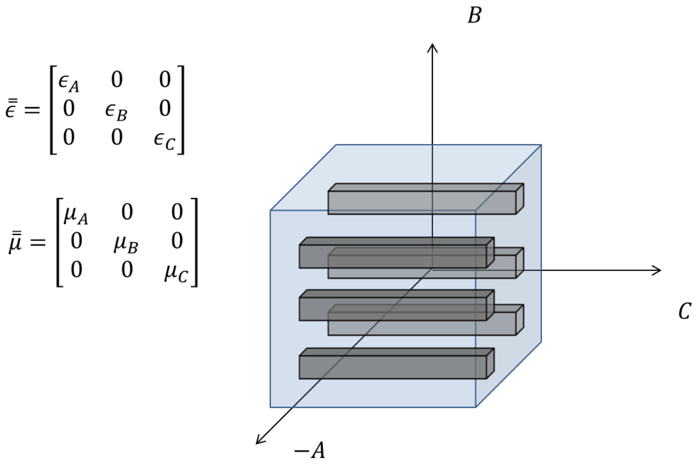

Figure 3.7: Biaxial material with Vias oriented along C axis. Figure taken from [5].

The first measurement configuration involves aligning the sample's B axis with the y excitation. The sample is placed in a position of $(A, B, C) \rightarrow (x.y.z)$ with respect to the RAW coordinate system shown in Fig. 3.8.

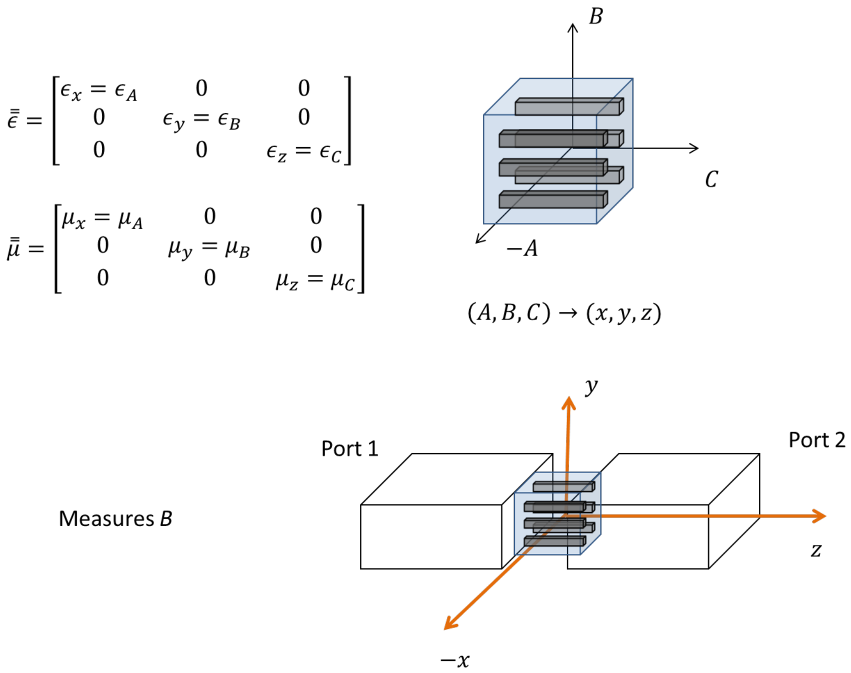

Figure 3.8: Excitation of sample's B axis. Figure taken from [5].

The second measurement once again places the sample's B axis in line with the excitation mode, but the sample is rotated such that $(A, B, C) \rightarrow (-z, y, x)$ as shown in Fig. 3.9. These first three measurements $(S_{11,1}, S_{21,1}, S_{21,2})$ allow for the extraction of 3 of the desired material parameters that will be designated as $\hat{\epsilon}_B, \hat{\mu}_A$ and $\hat{\mu}_C$. The hat represents an estimated parameter extracted from simulated measurements of the MUT.

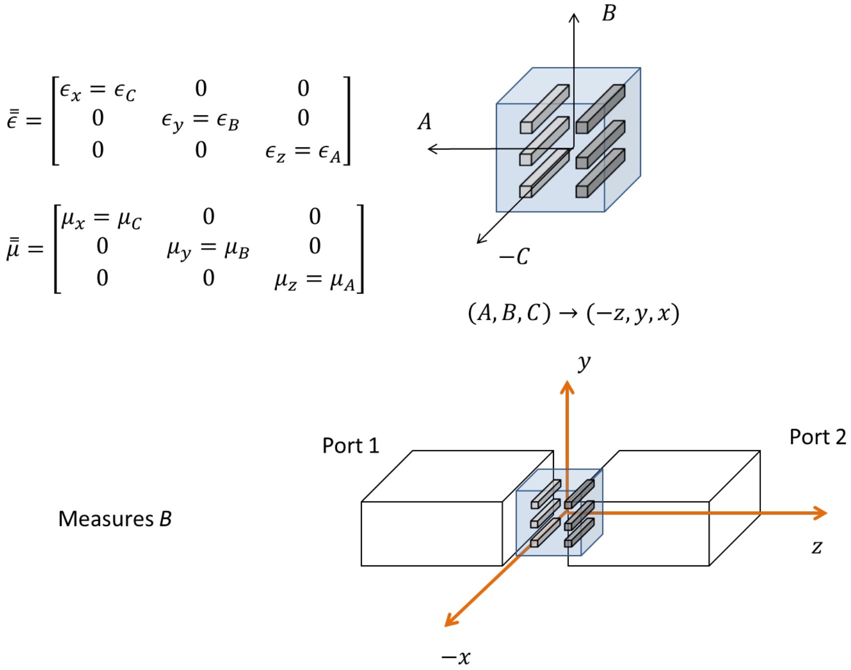

Figure 3.9: Second excitation of sample's B axis. Figure taken from [5].

The third orientation measured allows for the excitation of the A axis of the MUT by setting the alignment to be $(A, B, C) \rightarrow (y, -x, z)$ illustrated in Fig. 3.10. This configuration along with the use of $\hat{\mu}_C$ from the previous step allows for the extraction of $\hat{\epsilon}_A$ and $\hat{\mu}_B$.

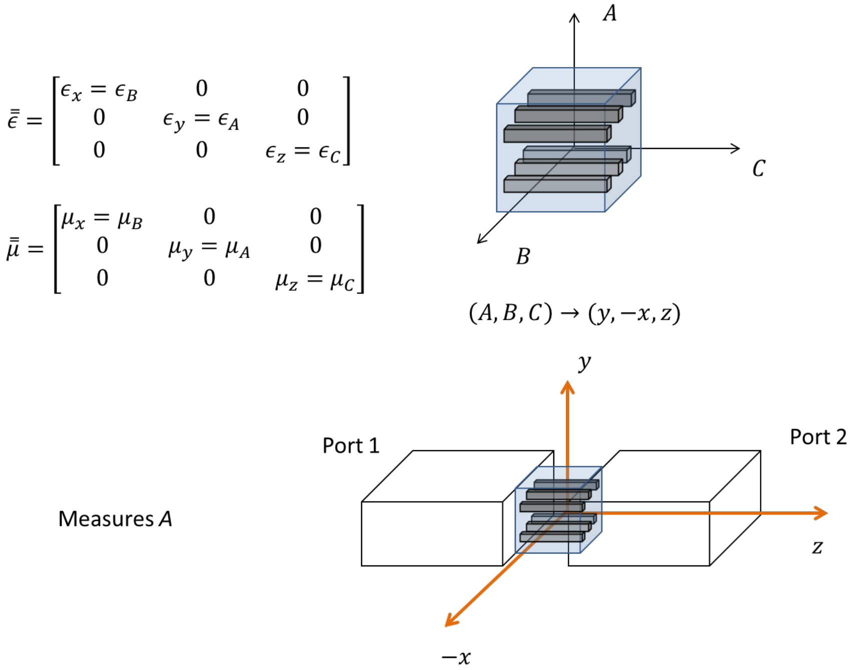

Figure 3.10: Excitation of sample's A axis. Figure taken from [5]

The fourth and final measurement excites the sample's C axis by placing it in a relative orientation of $(A, B, C) \rightarrow (z, x, y)$ as shown in Fig. 3.11. This orientation in conjunction with the use of $\hat{\mu}_A$ and $\hat{\mu}_B$ from previous steps allows for the extraction of the final complex parameter $\hat{\epsilon}_C$. A summary of these measurements and the parameters they are used to extract are listed in Table 3.2.

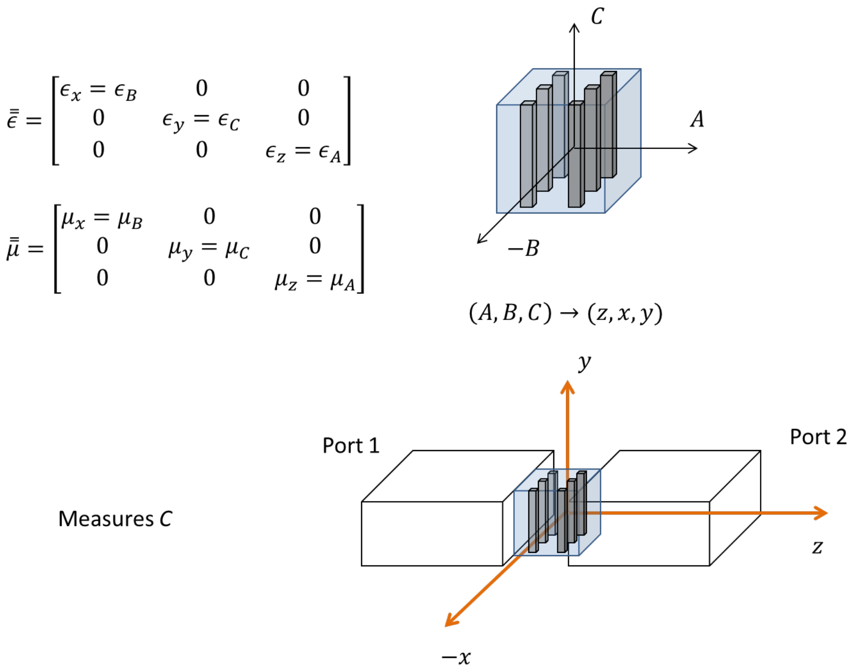

$$\bar{\bar{\epsilon}} = \begin{bmatrix} \epsilon_x = \epsilon_B & 0 & 0 \\ 0 & \epsilon_y = \epsilon_C & 0 \\ 0 & 0 & \epsilon_z = \epsilon_A \end{bmatrix}$$

$$\bar{\bar{\mu}} = \begin{bmatrix} \mu_x = \mu_B & 0 & 0 \\ 0 & \mu_y = \mu_C & 0 \\ 0 & 0 & \mu_z = \mu_A \end{bmatrix}$$

Figure 3.11: Excitation of sample's C axis. Figure taken from [5]

Configuration # (Figure)	Sample Orientation ($\epsilon_{yy}, \mu_{xx}, \mu_{zz}$)	Newton Method Formulation
1 (3.8)	(A,B,C) $\rightarrow (x, y, z)$	$\begin{bmatrix} S_{11}^{thy}(\epsilon_B, \mu_A, \mu_C) - S_{11,1}^{meas} \\ S_{21}^{thy}(\epsilon_B, \mu_A, \mu_C) - S_{21,1}^{meas} \\ S_{11}^{thy}(\epsilon_B, \mu_C, \mu_A) - S_{21,2}^{meas} \end{bmatrix} = \begin{bmatrix} 0 \\ 0 \\ 0 \end{bmatrix} \rightarrow [\hat{\epsilon_B}, \hat{\mu_A}, \hat{\mu_C}]$
1 (3.8)	(A,B,C) $\rightarrow (x, y, z)$	
2 (3.9)	(A,B,C) $\rightarrow (-z, y, x)$	
3 (3.10)	(A,B,C) $\rightarrow (y, -x, z)$	$\begin{bmatrix} S_{11}^{thy}(\epsilon_A, \mu_B, \hat{\mu_C}) - S_{11,3}^{meas} \\ S_{21}^{thy}(\epsilon_A, \mu_B, \hat{\mu_C}) - S_{21,3}^{meas} \end{bmatrix} = \begin{bmatrix} 0 \\ 0 \end{bmatrix} \rightarrow [\hat{\epsilon_A}, \hat{\mu_B}]$
3 (3.10)	(A,B,C) $\rightarrow (y, -x, z)$	
4 (3.11)	(A,B,C) $\rightarrow (z, x, y)$	$\begin{bmatrix} S_{21}^{thy}(\epsilon_C, \hat{\mu_A}, \hat{\mu_B}) - S_{21,4}^{meas} \end{bmatrix} = [0] \rightarrow [\hat{\epsilon_C}]$

Table 3.2: A summary of the measurement orientations and the corresponding parameter extraction.

3.3.1 Cost Function

The measurements described in Section 3.3 can support a set of complex non-linear cost functions

$$\begin{aligned}
S^{thy}_{11,A}(\mathbf{f};\bar{\bar{\epsilon}},\bar{\bar{\mu}}) - S^{meas}_{11,A}(\mathbf{f}) &= \delta_A \\
S^{thy}_{21,A}(\mathbf{f};\bar{\bar{\epsilon}},\bar{\bar{\mu}}) - S^{meas}_{21,A}(\mathbf{f}) &= \gamma_A \\
S^{thy}_{11,B}(\mathbf{f};\bar{\bar{\epsilon}},\bar{\bar{\mu}}) - S^{meas}_{11,B}(\mathbf{f}) &= \delta_B \\
S^{thy}_{21,B}(\mathbf{f};\bar{\bar{\epsilon}},\bar{\bar{\mu}}) - S^{meas}_{21,B}(\mathbf{f}) &= \gamma_B \\
S^{thy}_{11,C}(\mathbf{f};\bar{\bar{\epsilon}},\bar{\bar{\mu}}) - S^{meas}_{21,C}(\mathbf{f}) &= \delta_C \\
S^{thy}_{21,C}(\mathbf{f};\bar{\bar{\epsilon}},\bar{\bar{\mu}}) - S^{meas}_{21,C}(\mathbf{f}) &= \gamma_C
\end{aligned} \tag{3.2}$$

which may be used to estimate the complex material tensors. In (3.2)$\{\delta_A, \delta_B, \delta_C, \gamma_A, \gamma_B, \gamma_C\}$ are tolerances for the cost functions. Minimization is accomplished using non-linear unconstrained minimization. Despite the complex nature of the simulated S-Parameters real-valued cost functions can be developed by considering the magnitude of the differences between the simulated (measured) and analytic values. The cost function for the first stage listed in Table 3.2 is given as [5]

$$\begin{gathered}
g(\vec{x}) = |S^{thy}_{11}(f;\vec{x}) - S^{meas}_{11,1}(f)| + |S^{thy}_{21}(f;\vec{x}) - S^{meas}_{21,1}(f)| + |S^{thy}_{21}(f;\vec{x}\,') - S^{meas}_{11,2}(f)| \\
\vec{x} = [x_1, x_2, x_3, x_4, x_5, x_6] = [\epsilon_{B,R}, \epsilon_{B,I}, \mu_{A,R}, \mu_{A,I}, \mu_{C,R}, \mu_{C,I}] \\
\vec{x}\,' = [x_1, x_2, x_5, x_6, x_3, x_4] = [\epsilon_{B,R}, \epsilon_{B,I}, \mu_{C,R}, \mu_{C,I}\mu_{A,R}, \mu_{A,I}] \\
\hat{x} = \underset{x_1,x_2,x_3,x_4,x_5,x_6}{argmin}\; g(\vec{x})
\end{gathered} \tag{3.3}$$

with $\mu = \mu_R - j\mu_I$ and $\epsilon = \epsilon_R - j\epsilon_I$. Equation (3.3) allows for the estimation of the material parameters $\hat{\epsilon}_B$, $\hat{\mu}_A$, and $\hat{\mu}_C$. It should be noted that $\vec{x}$ and $\vec{x}'$ are comprised of the same values but in different orders. For this reason only $\vec{x}$ is solved for in (3.3).

The cost function for the second step of the extraction process is

$$
\begin{gathered}
g(\vec{x}) = |S_{11}^{thy}(f;\vec{x}) - S_{11,3}^{meas}(f)| + |S_{21}^{thy}(f;\vec{x}) - S_{21,3}^{meas}(f)| \\
\vec{x} = [x_1, x_2, x_3, x_4, x_5, x_6] = [\epsilon_{A,R}, \epsilon_{A,I}, \mu_{B,R}, \mu_{B,I}, \hat{\mu}_{C_R}, \hat{\mu}_{C,I}]\hat{x} = \underset{x_1,x_2,x_3,x_4}{argmin}\, g(\vec{x})
\end{gathered}
\tag{3.4}
$$

and solves for $(\hat{\epsilon}_A, \hat{\mu}_B)$ when the function is minimized.

The final cost function to extract the value of ϵ_C is

$$
\begin{gathered}
g(\vec{x}) = |S_{21}^{thy}(f;\vec{x}) - S_{21,4}^{meas}(f)| \\
\vec{x} = [\epsilon_{C,R}, \epsilon_{C,I}, \hat{\mu}_{A,R}, \hat{\mu}_{A,I}, \hat{\mu}_{B,R}, \hat{\mu}_{B,I}] \\
\hat{x} = \underset{x_1,x_2}{argmin}\, g(\vec{x})
\end{gathered}
\tag{3.5}
$$

Clearly, the aggregate estimation errors for $\hat{\epsilon}_A, \hat{\epsilon}_B, \hat{\mu}_A, \hat{\mu}_B, \hat{\mu}_C$ will influence the accuracy on $\hat{\epsilon}_C$.

These cost functions require an initial guess of dielectric properties. The optimization algorithm searches for values near the initial guess until g is minimized or a maximum number of searches occurs. The algorithm is supervised, meaning that the user must decide to keep something near the last result or to start with a new initial guess for each frequency. However, the material properties are expected to be slowly varying with frequency, so the reult of the previous frequency can be used for the current search. A specific example of the procedure pertaining to the experiment project is outlined in Section 3.3.2

3.3.2 Procedure

The first step to apply the experimental design in this research project will use to extract parameters that will be used in the analysis of dielectric properties with respect to the changes made to the air filled vias. This step was described in Section 3.2. The second stage is to complete the full wave simulation using the model in Section 3.1, Fig. 3.4. The third stage is to evaluate the cost functions given in Section 3.3.1. The mode matching solution of Section 2.2.2 serves as the theoretical results in the non-linear unconstrained minimization function. The optimization algorithm is implemented in MATLAB and uses non-linear least squares.

3.3.3 Verification of Parameter Extraction

The verification of the parameter extraction process is completed by filling the sample region with free space and performing the procedure outlined in Section 3.3.2. The expected parameter estimation has an expected isotropic permittivity taking the form of

$$\bar{\bar{\epsilon}} = \bar{\bar{I}}\epsilon \tag{3.6}$$

and permeability

$$\bar{\bar{\mu}} = \bar{\bar{I}}\mu \tag{3.7}$$

where $\epsilon = \epsilon_r \epsilon_0$ and $\mu = \mu_r \mu_0$. In the case of free space $\epsilon_r = \mu_r = 1$.

Figure 3.12 to Fig. 3.14 shows the estimated permittivity $(\hat{\epsilon}_A, \hat{\epsilon}_B, \hat{\epsilon}_C)$ for the air-filled sample holder. As can be seen the permittivity provided by the air sample is consistent with the permittivity of free space.

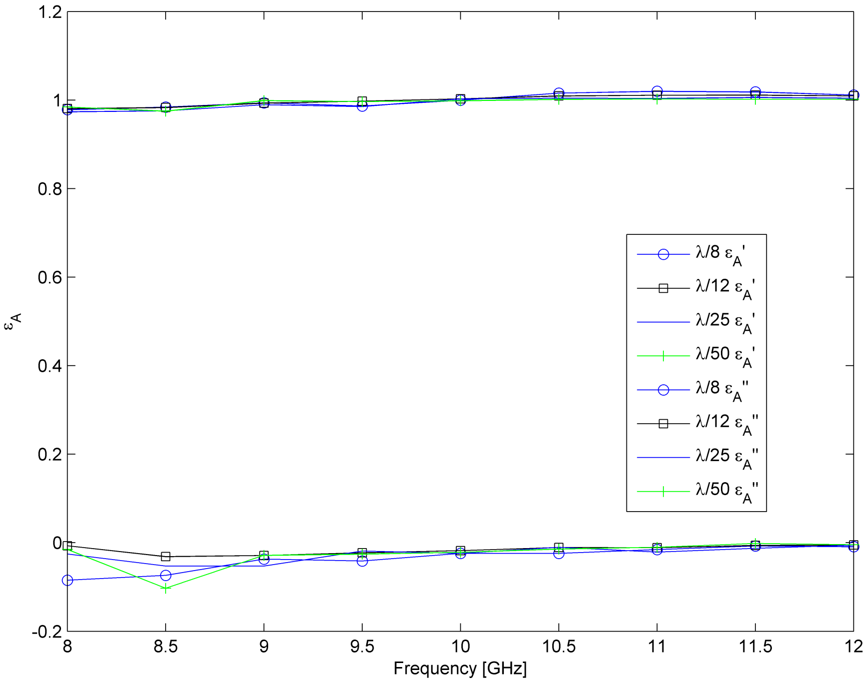

Figure 3.12: Extracted ϵ_A for air-filled reduced aperture structure with full wavelength of waveguide before and after sample holder.

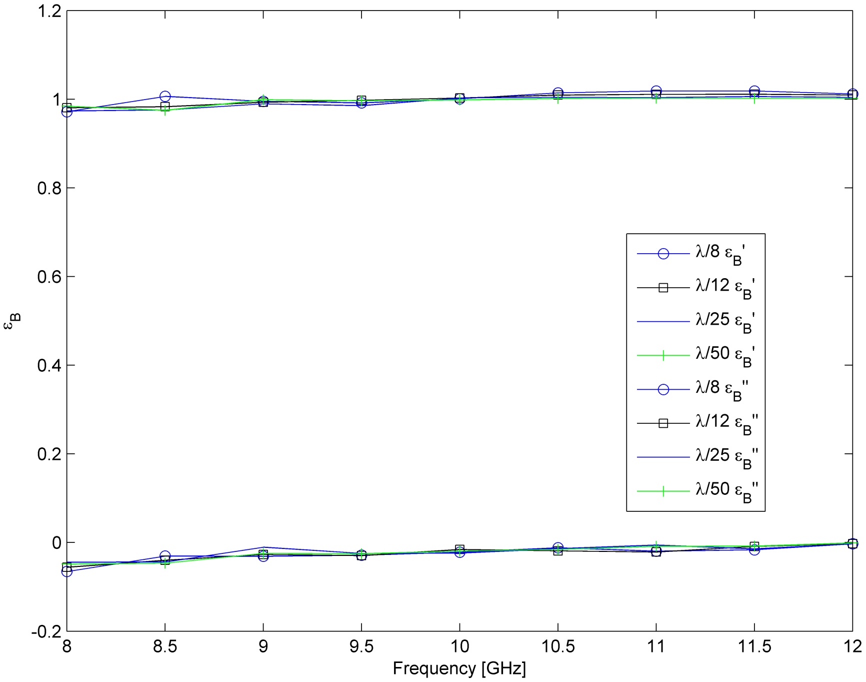

Figure 3.13: Extracted ϵ_B for air-filled reduced aperture structure with full wavelength of waveguide before and after sample holder.

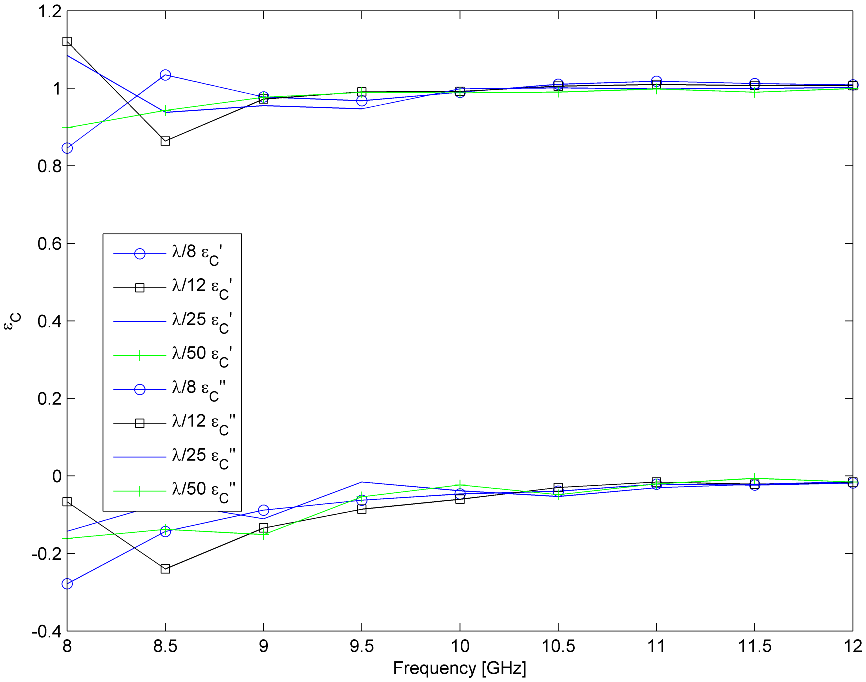

Figure 3.14: Extracted ϵ_C for air-filled reduced aperture structure with full wavelength of waveguide before and after sample holder.

Figures 3.15 to 3.17 shows the estimated permeability ($\hat{\mu}_A, \hat{\mu}_B, \hat{\mu}_C$) and agrees with the non-magnetic nature of free-space..

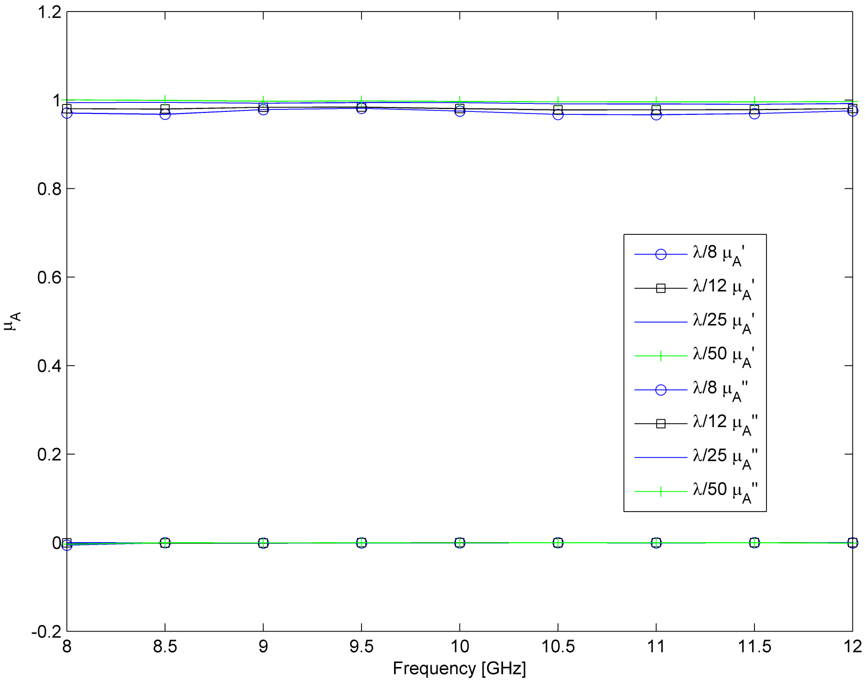

Figure 3.15: Extracted μ_A for air-filled reduced aperture structure with full wavelength of waveguide before and after sample holder.

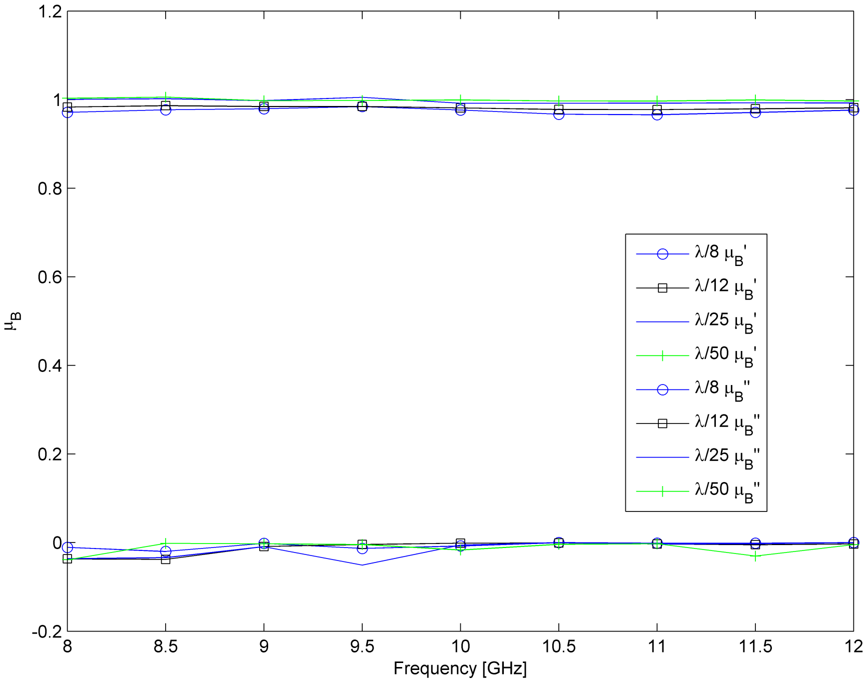

Figure 3.16: Extracted μ_B for air-filled reduced aperture structure with full wavelength of waveguide before and after sample holder.

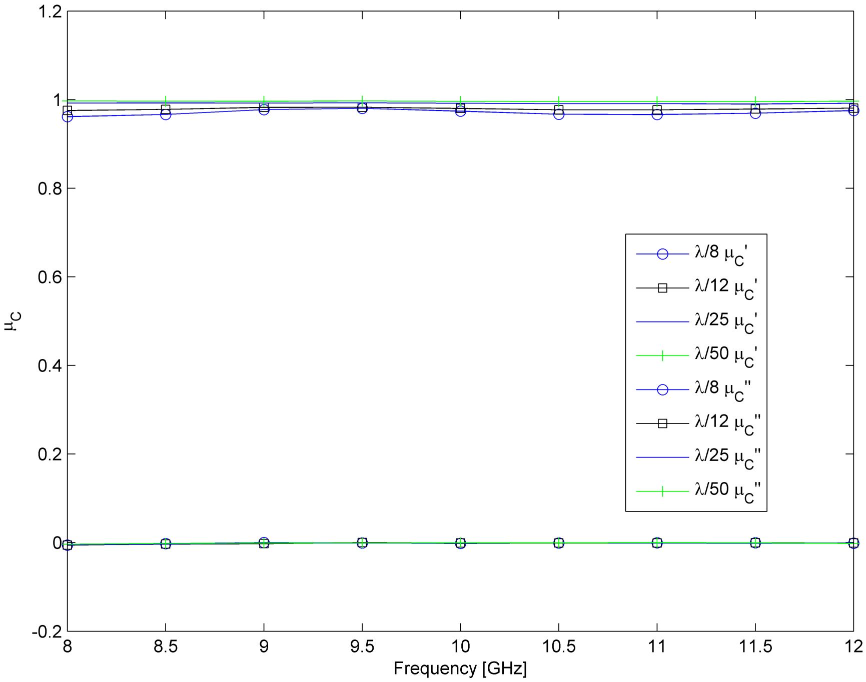

Figure 3.17: Extracted μ_C for air-filled reduced aperture structure with full wavelength of waveguide before and after sample holder.

Results

The bulk material used in the simulated experiment in this section has the properties of lossless, simple media with $\epsilon_r = 2.8 - j0$ and $\mu_r = 1 - j0$. The procedure was run as outlined in Section 3.3.2. The parameter estimation process was repeated 10 times for each trial and the results were averaged. This repetition allowed some insight into the accuracy of the material estimation program.

4.1 Via Size and Spacing

For the purpose of examining the effects that size and spacing of the machined vias have on the final estimated parameters, 24 trials listed in Table 3.1 were modeled and simulated.

Figures 4.1 - 4.3 show the electric permittivity along the 3 cardinal axes which are subscripted A, B, and C. Only results at 8, 9, 10, and 11 GHz are shown. The ϵ_A (Fig. 4.1) and ϵ_B (Fig. 4.2) have very similar behavior which is to be expected due to the symmetry of the air via lattices as shown in the example lattice in Figure 1.5. However, when looking at the permittivity along the asymmetric axis (Fig. 4.3) the permittivity shows slightly different characteristics. In all three of the cases it can be seen that the imaginary part of the permittivity is very close to zero which shows that the loss less property of the base dielectric material is preserved. In all three cases it can be seen that when the test sample is 96% material and 4% air the real part of the permittivity only reduces to 2.7008 or the equivalent of 97.5% of the original material permittivity. The outliers near $\frac{1}{\rho} = 3$ appear for certain frequencies can be explained by resonances created by the vias [9].

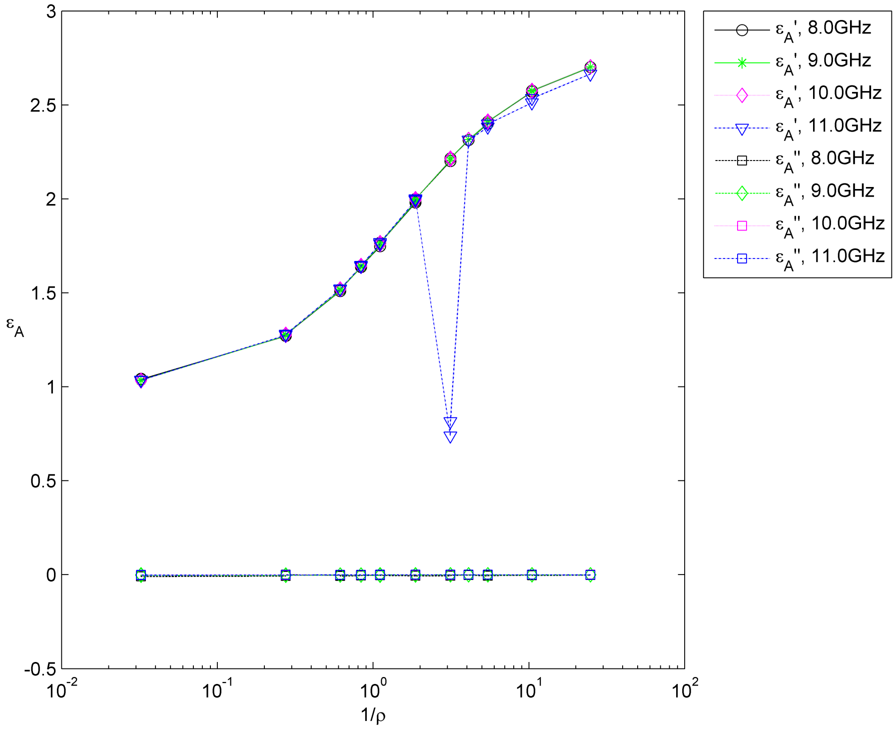

Figure 4.1: Complex permittivity along A axis versus air-to-dielectric ratio(ρ).

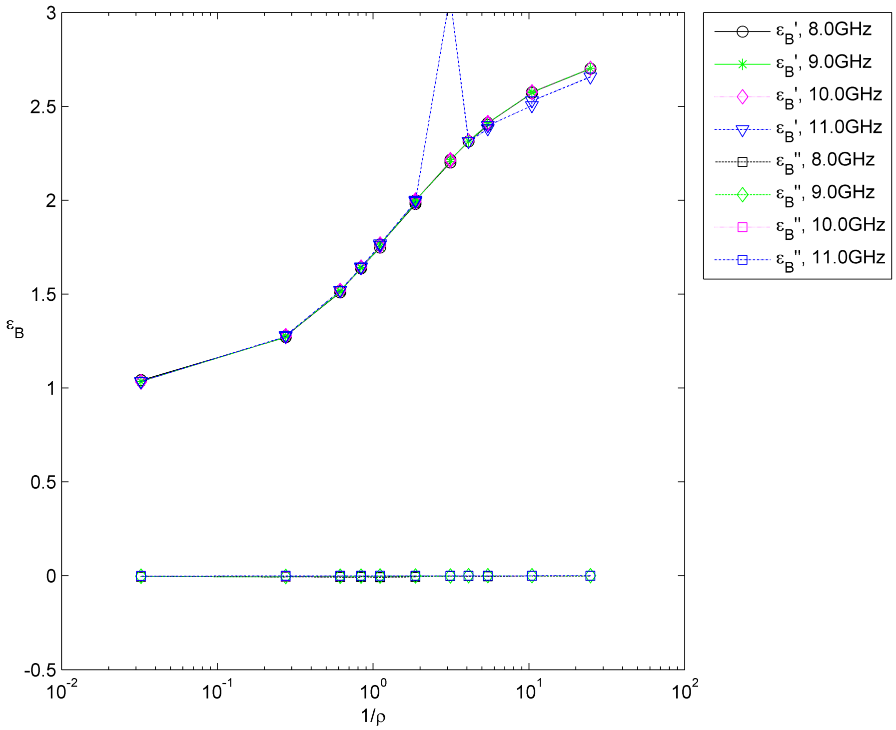

Figure 4.2: Complex permittivity along B axis versus air-to-dielectric ratio(ρ).

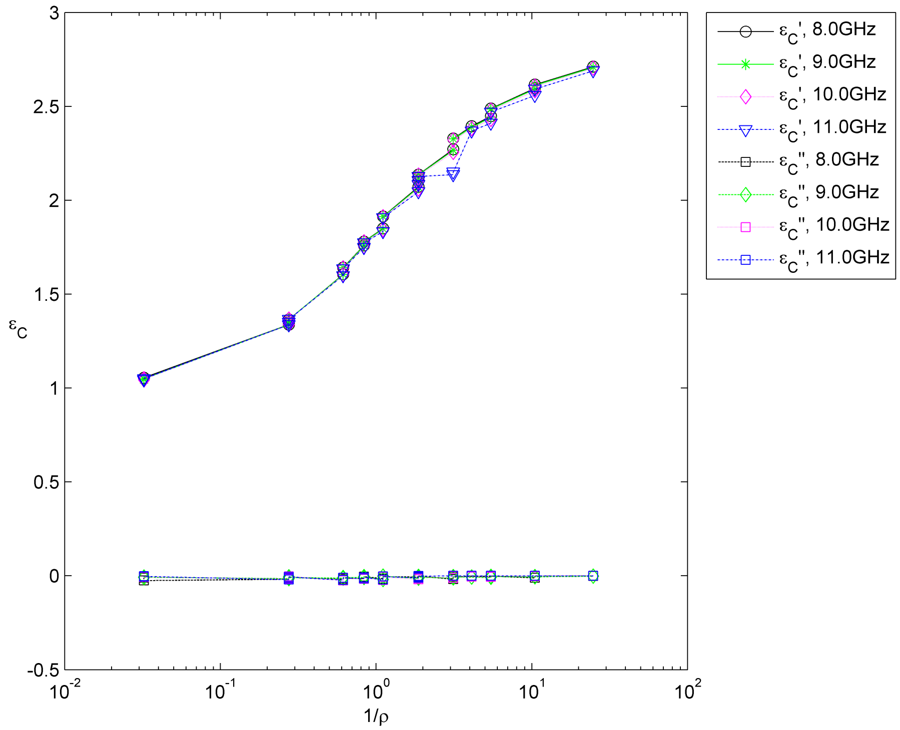

Figure 4.3: Complex permittivity along C axis versus air-to-dielectric ratio(ρ).

Figures 4.4 to 4.6 show the complex permeability along the three cardinal axes (A, B, C). These provide insight as to how change in the lattice structure affects the non-magnetic qualities of the base material. It can be seen that varying the size, spacing, and ratio of air-to-dielectric ratio of the material has no effect on the permeability of the structure. It retains the property of $\mu_{r,fs} = \mu_{r,sample}$.

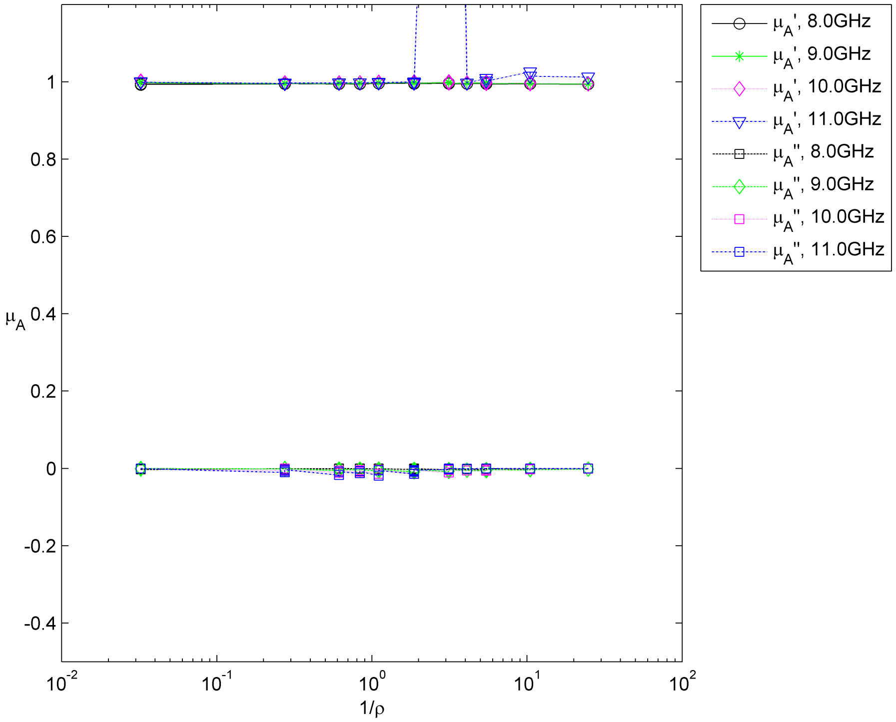

Figure 4.4: Complex permeability along A axis versus air-to-dielectric ratio(ρ).

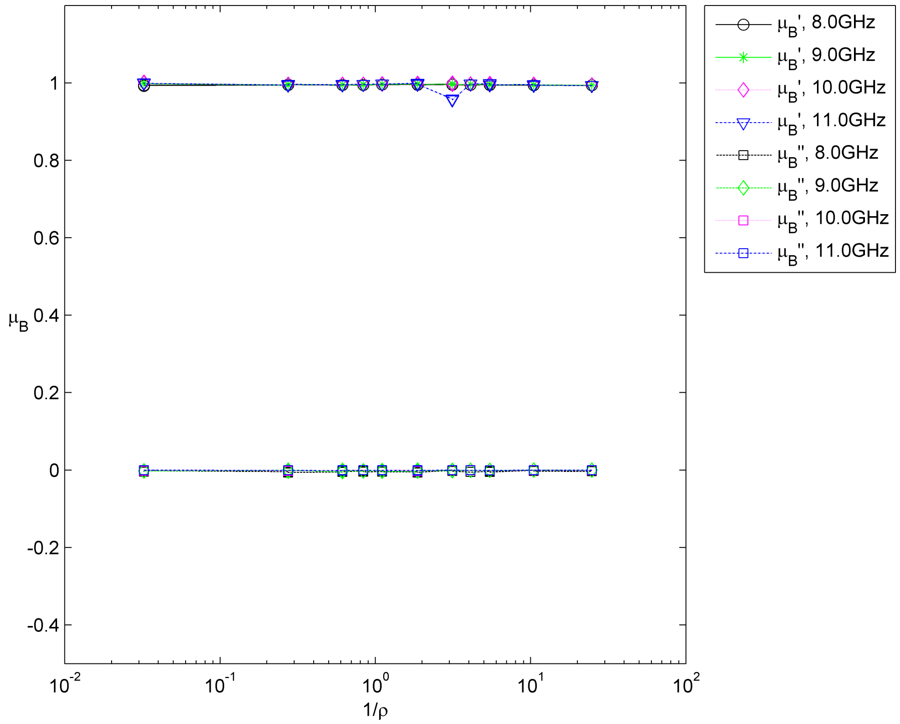

Figure 4.5: Complex permeability along A axis versus air-to-dielectric ratio(ρ).

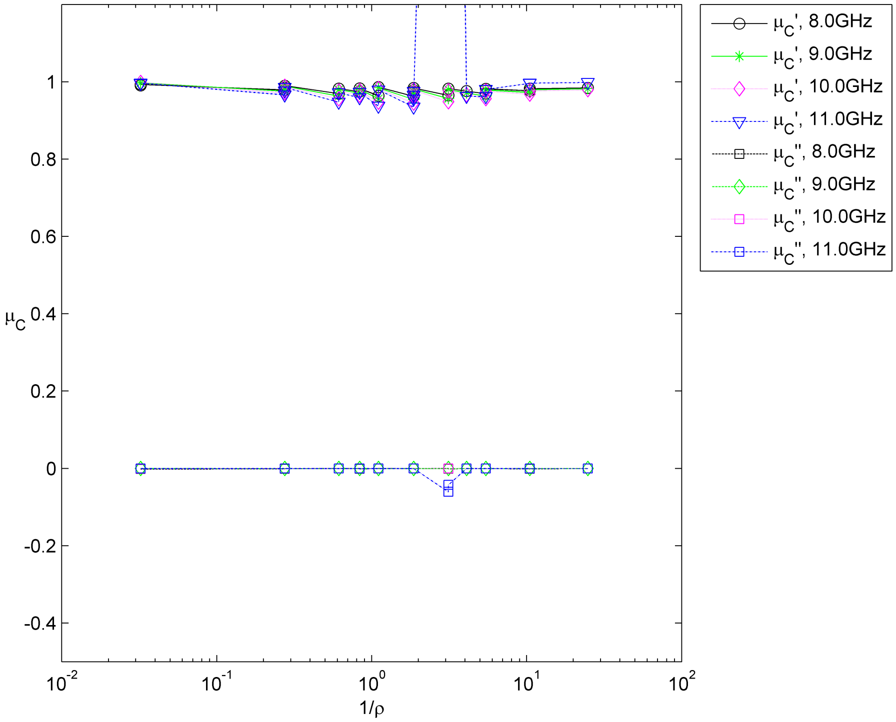

Figure 4.6: Complex permeability along A axis versus air-to-dielectric ratio(ρ).

Another observation can be made by examination of Fig. 4.1 to 4.6 is that the via size and separation do not cause any frequency selectivity to be created in the metamaterial structure.

Due to the material showing almost no variation due to frequency the following analysis is at the center frequency of the band (10 GHz) but should be assumed valid for any frequency in the band (8-12 GHz). Figure 4.7 shows the reaction of the material property $\hat{\epsilon}_A$ with respect to ρ for the parameter estimation. Standard deviation bounds are also shown about the mean. The variation of the individual parameter estimations is very small. This would indicate that near the global minimum of the cost function, the hyperplanes are very smooth causing the algorithm to find virtually the same values for the estimated parameters each time.

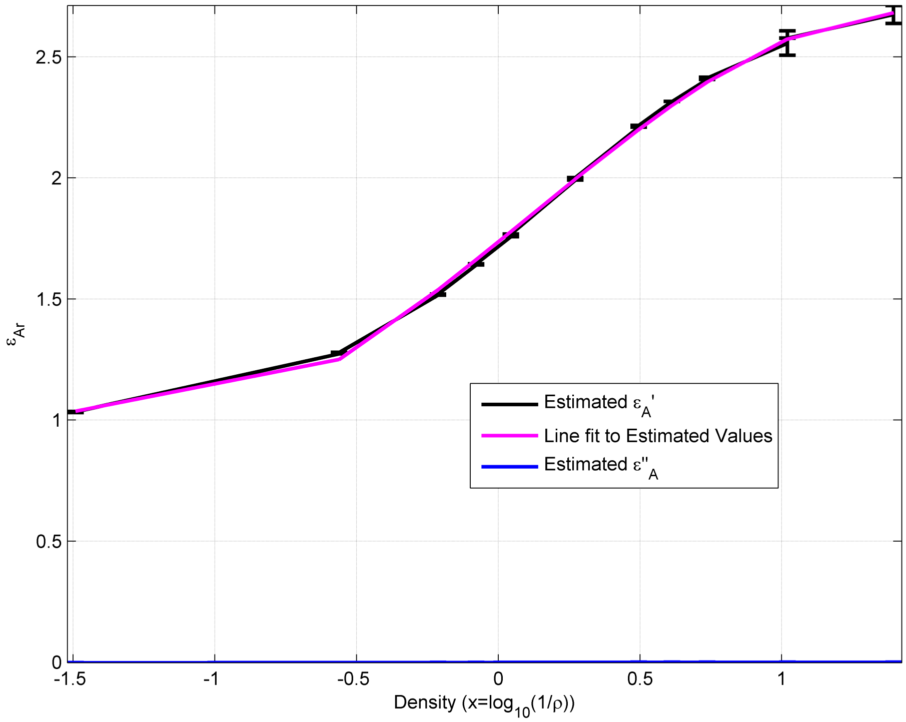

Figure 4.7: Complex permittivity along A axis versus air-to-dielectric ratio (ρ) for 10 GHz.

Utilizing MATLAB's curve fitting tool a formula for the estimated material property ($\hat{\epsilon}_A = \hat{\epsilon}'_A - j\hat{\epsilon}''_A$) is given as

$$\hat{\epsilon}'_A = -0.18067x^3 + 0.055116x^2 + 0.95278x + 1.7366 \tag{4.1}$$

$$\hat{\epsilon}''_A = 0 \tag{4.2}$$

where x is defined as $\log 10(\frac{1}{\rho})$ and ρ is defined as (3.1).

Similarly, Fig. 4.8 shows the estimated values of $\hat{\epsilon_B}$ as

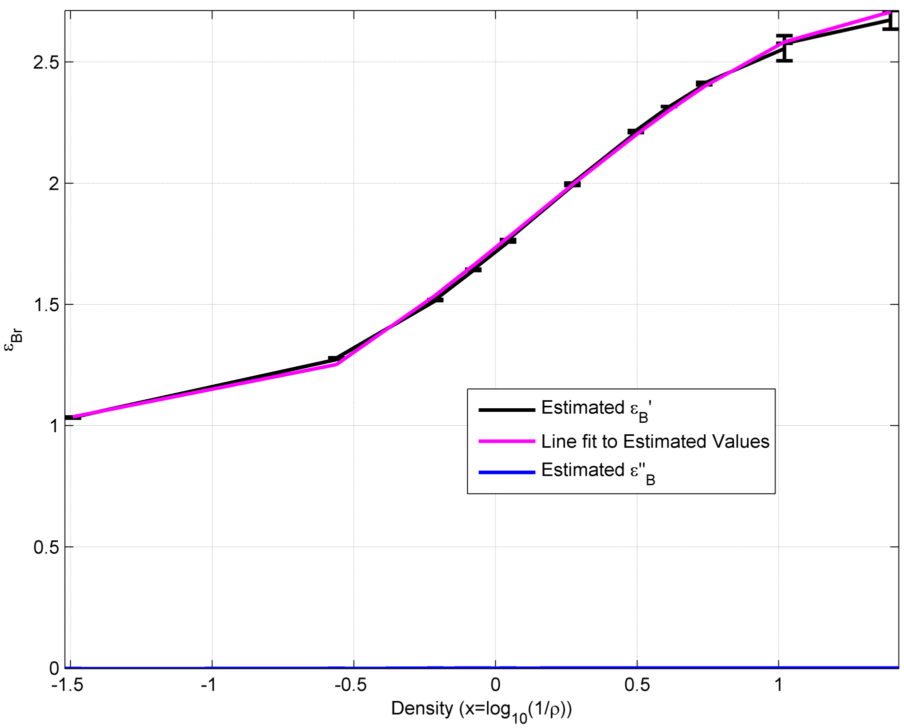

Figure 4.8: Complex permittivity along B axis versus air-to-dielectric ratio (ρ) for 10 GHz.

$$\hat{\epsilon}'_B = -0.17462x^3 + 0.062365x^2 + 0.94968x + 1.7354 \tag{4.3}$$

$$\hat{\epsilon}''_B = 0. \tag{4.4}$$

Finally, $\hat{\epsilon}_C$ has a similar trend

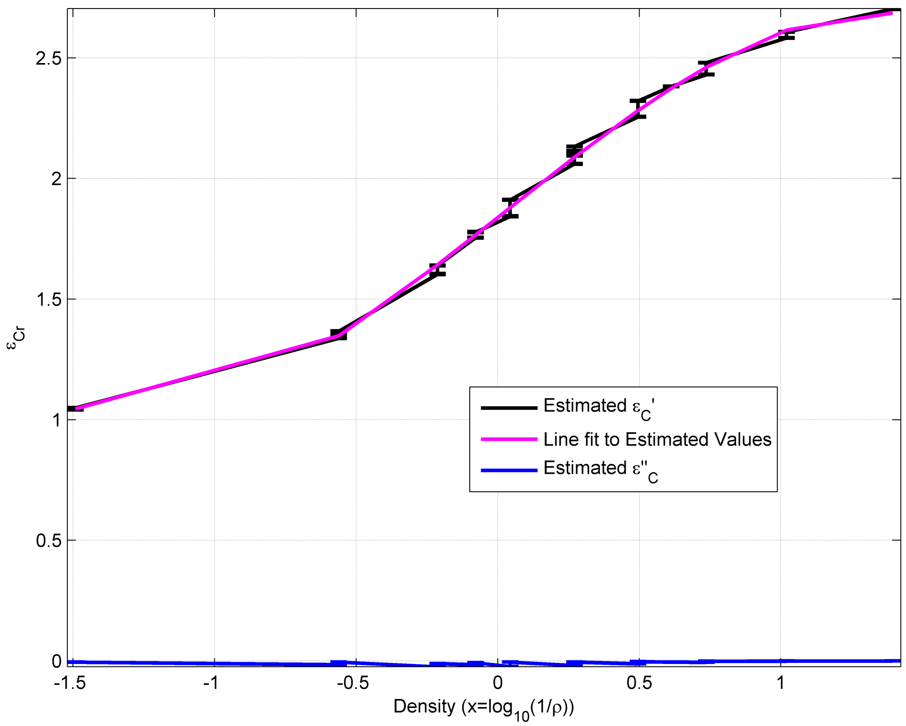

Figure 4.9: Complex permittivity along C axis versus air-to-dielectric ratio (ρ) for 10 GHz.

$$\hat{\epsilon}'_C = -0.17404x^3 + 0.0094338x^2 + 0.93314x + 1.8385 \tag{4.5}$$

$$\hat{\epsilon}''_C = 0. \tag{4.6}$$

While the general shape of all three property graphs is similar it should be noted that the variance of $\hat{\epsilon}_C$ is higher than the other two properties. This is due to the fact that it is the final property to be extracted as seen on 3.2. This means that any error that is in the system is compounded upon each step of the process causing greater variation in the properties that are estimated at the end.

As seen before and confirmed in figures 4.10 to 4.12 neither the size nor the spacing of the elements of the lattice cause the material to show a magnetic response assuming that the starting material is non-magnetic.

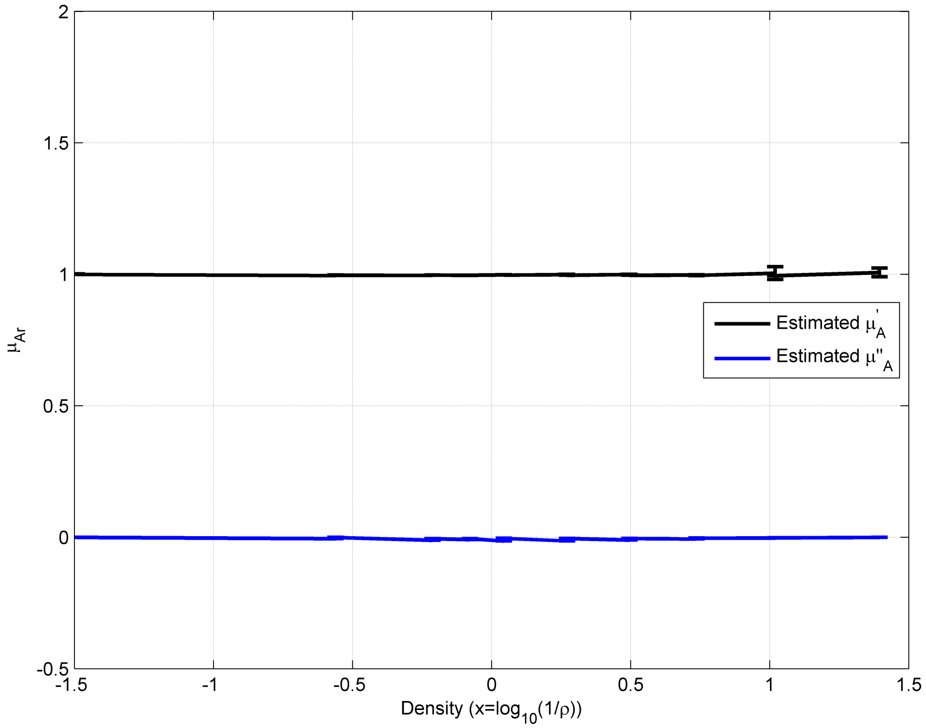

Figure 4.10: Complex permeability along A axis versus air-to-dielectric ratio (ρ) for 10 GHz.

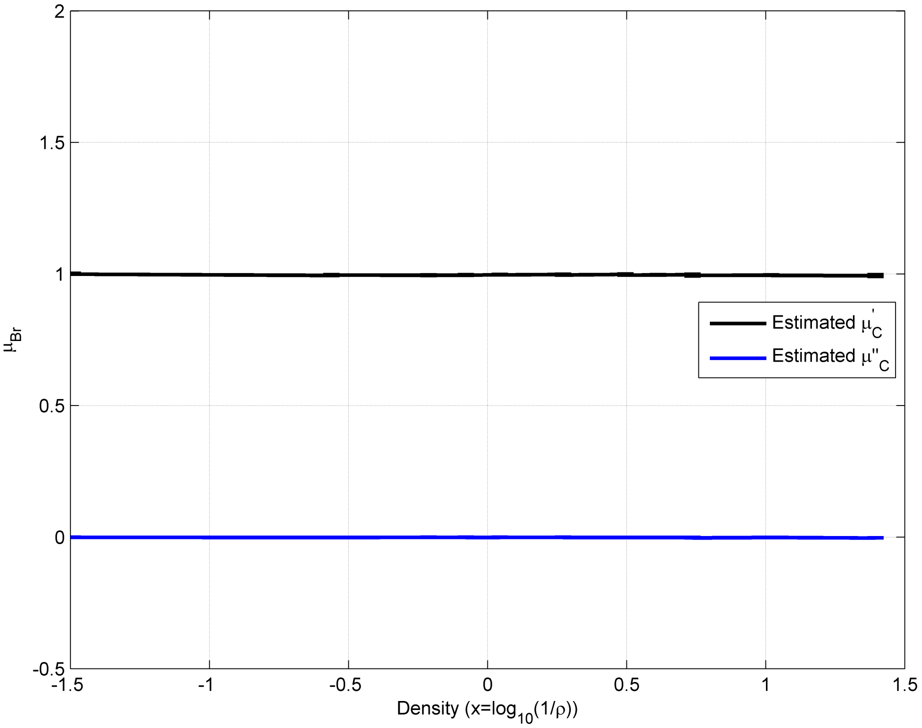

Figure 4.11: Complex permeability along B axis versus air-to-dielectric ratio (ρ) for 10 GHz.

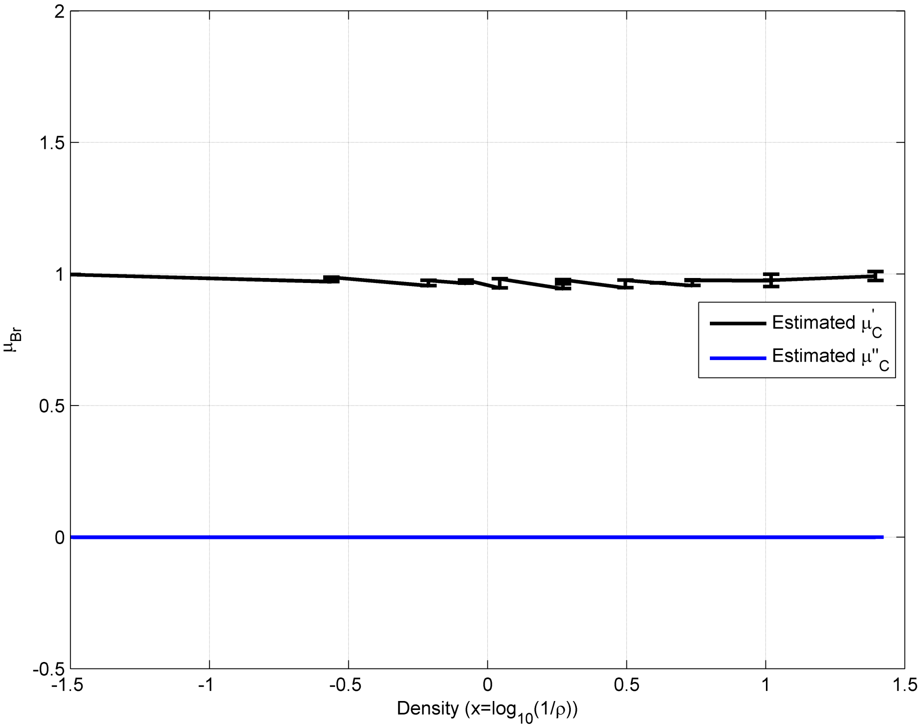

Figure 4.12: Complex permeability along C axis versus air-to-dielectric ratio (ρ) for 10 GHz.

A further examination that would be beneficial would be to change the ratio of via size in the A and B directions. The expectation for the material properties is that ϵ_A and μ_A will have properties agreeing with the air-to-dielectric ratio in the A direction. While, ϵ_B and $\mu_B$will have properties agreeing with the air-to-dielectric ratio in the B direction. Finally, ϵ_C and μ_C will be defined from the total density considering both the A and B densities.

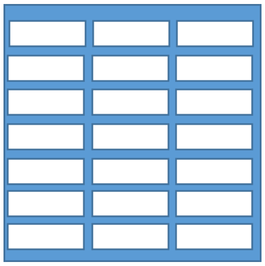

Figure 4.13: A test sample with rectangular vias with a side ratio of 3 to 1.

4.2 Rectangular Via

The next set of results to explore the effects that rectangular vias will have on the anisotropic nature of the material properties as opposed to the square vias used in the previous section. To explore these effects an experiment was designed that would extract the properties from materials that were designed with vias that have a ratio of 3 to 1 for the length of the sides along the A and B axis. This experiment used measurements of $1.53\ mm$ and $.51\ mm$ with respect to the axis creating the material sample shown in Fig. 4.13. The results of the parameter estimation process are shown in figures 4.14 to 4.16. The resulting material parameters are then analyzed by using the ratio of air-to-dielectric along the n axis (A, B, C) as

$$\begin{aligned} \rho_n &= \frac{\delta_n N_n}{l_n} \\ n &= A, B \end{aligned} \tag{4.7}$$

and

$$\rho_C = \rho_A \rho_B \tag{4.8}$$

with δ_n being the length of the air via along the n axis, N_n the number of vias along the n axis, and l_n the length of the sample along the n axis.

As was seen in results given earlier the via sizes have no effect on the material permeability and does not cause the material to take on a lossy nature. Due to this only the real part of the permittivity will be explored in this section. Figure 4.14 shows the real permittivity along the A axis (ϵ_{AA}) with respect to density changes in the A, B, and C axes.

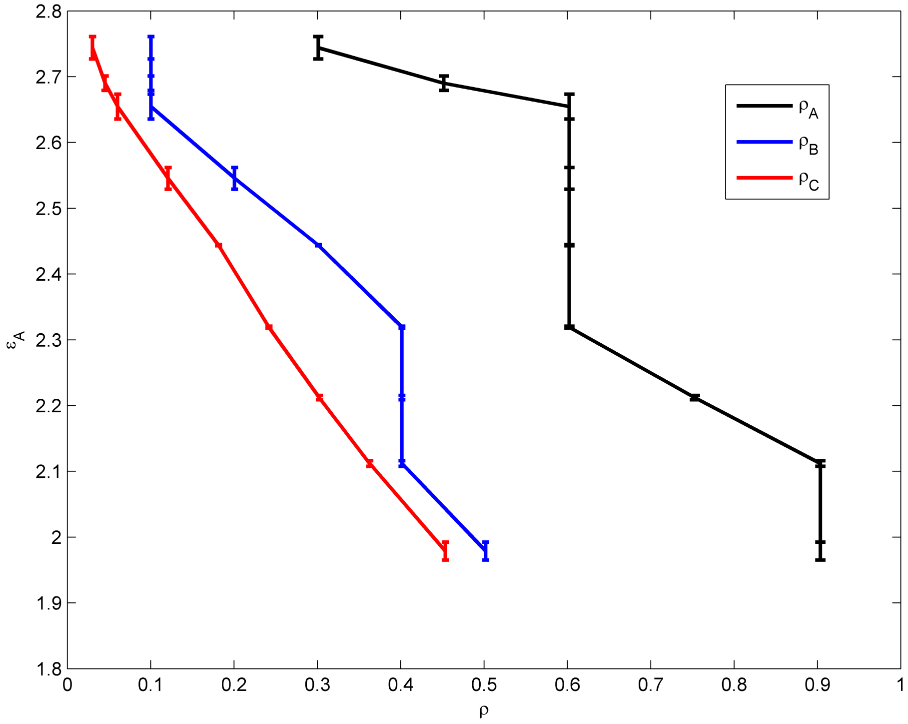

Figure 4.14: Real permittivity along the A axis a 3 to 1 rectangular via.

Similarly, Fig. 4.15 shows the real permittivity along the B (ϵ_{BB}) axis as

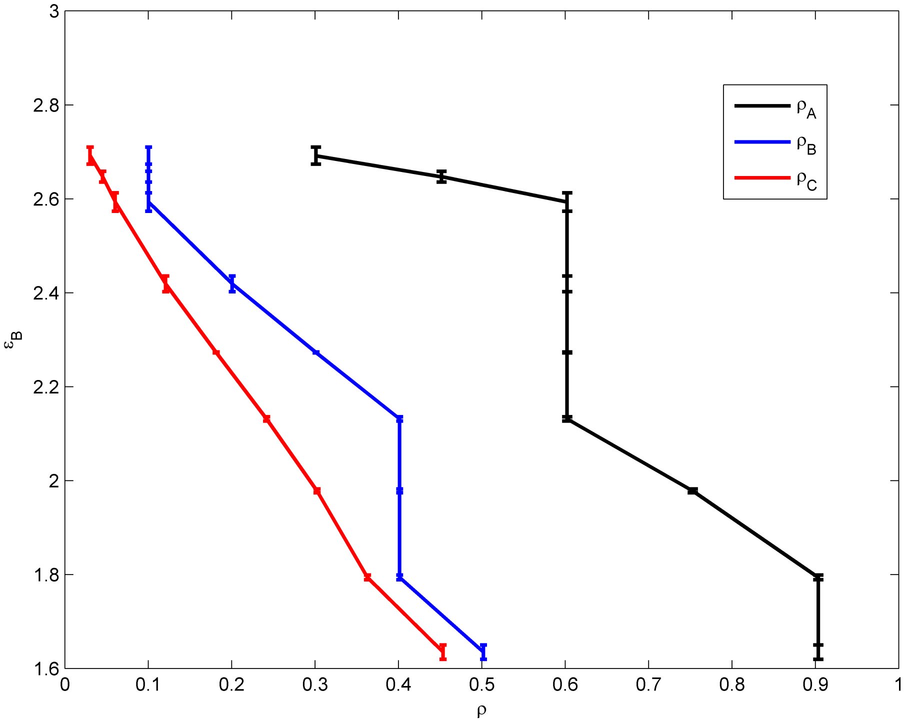

Figure 4.15: Real permittivity along the B axis a 3 to 1 rectangular via.

and Fig. 4.16 shows the real permittivity along the C axis (ϵ_{CC}) as

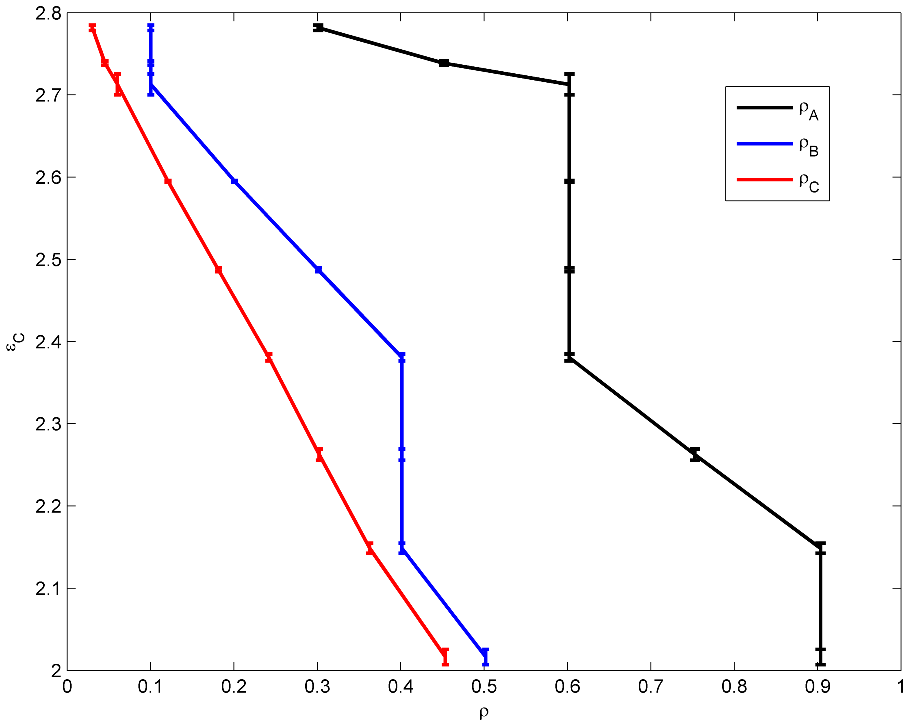

Figure 4.16: Real permittivity along the C axis a 3 to 1 rectangular via.

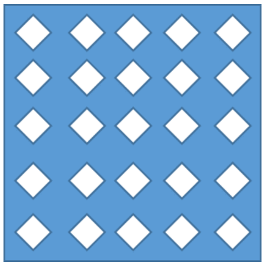

Figure 4.17: A test sample with the pose of the vias set to 45°.

4.3 Via Pose

To test the pose of the vias, a simulation was made with a value of $\rho = 0.54$ and no rotation. The vias were then rotated about their their center points to angles of 15, 30, and 45 Fig. (4.17). No measurements were taken beyond 45 degrees because of symmetry of the vias.

As can be seen in figures 4.18 to 4.20 the pose of a square via has no effect on the material permittivity. This can be explained by the fact that the dimensions of the air vias ($1\ mm\ x\ 1\ mm$) are electrically much smaller than the wavelength of the excitation wave (3 cm). The results shown by the variations in pose of the vias are beneficial in manufacturing as it removes the sensitivity of the machining process and small variations in the rotation of the individual elements of the lattice structure.

Likewise, Figures 4.21 to 4.23 shows the pose has no effect on the permeability.

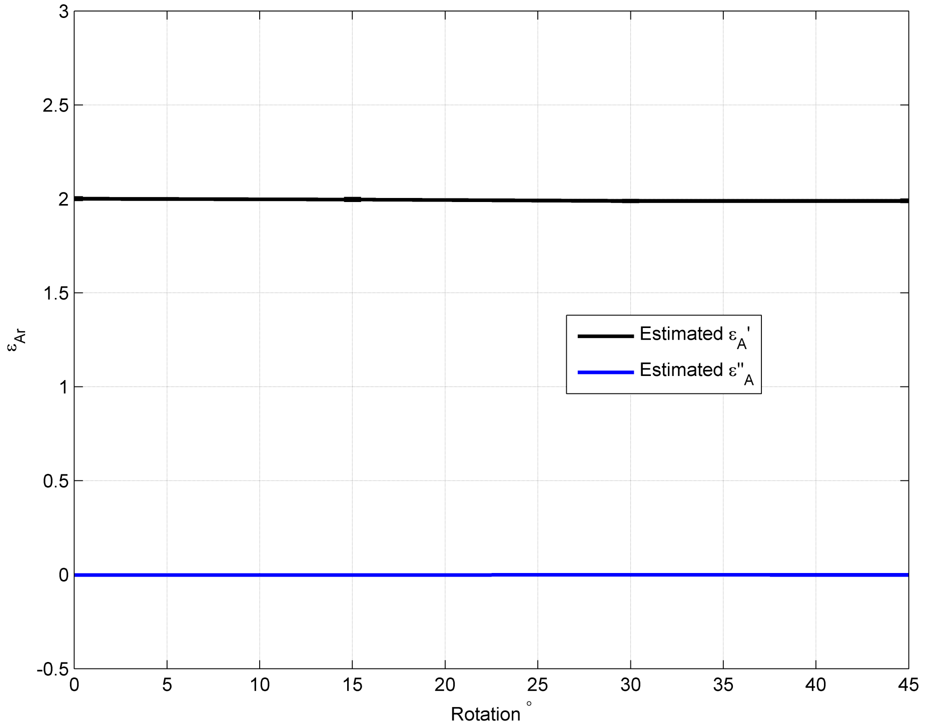

Figure 4.18: Complex permittivity along A axis compared to rotation.

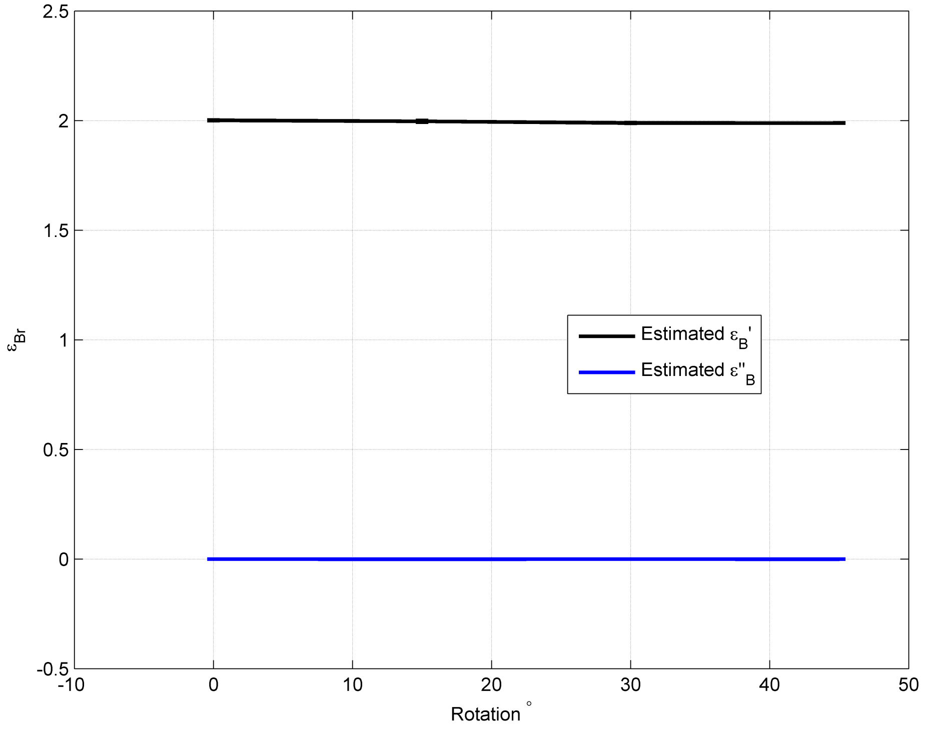

Figure 4.19: Complex permittivity along B axis compared to rotation.

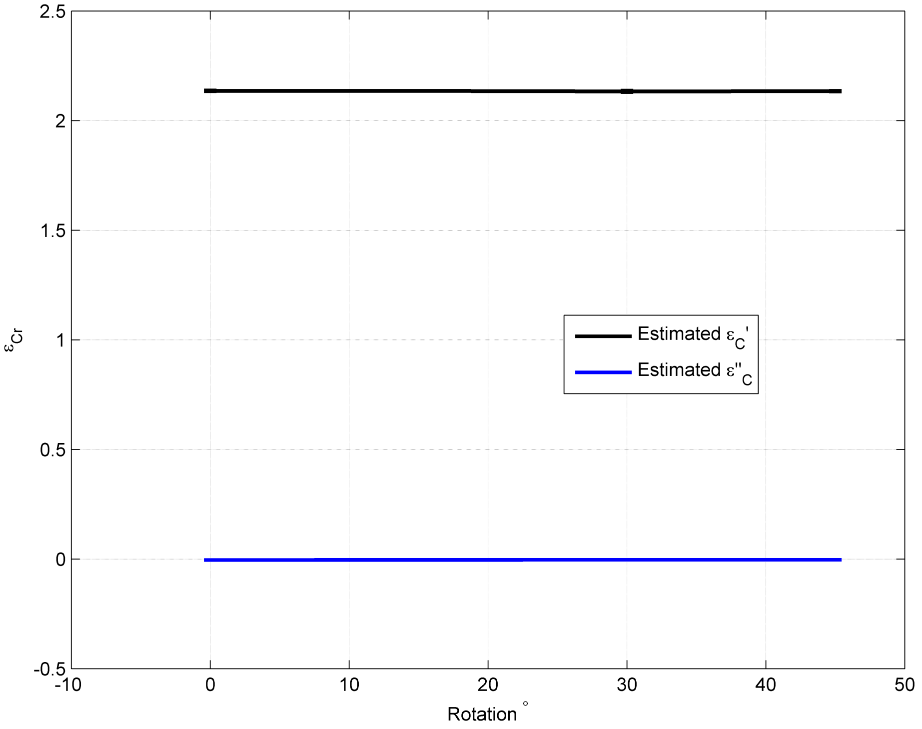

Figure 4.20: Complex permittivity along C axis compared to rotation.

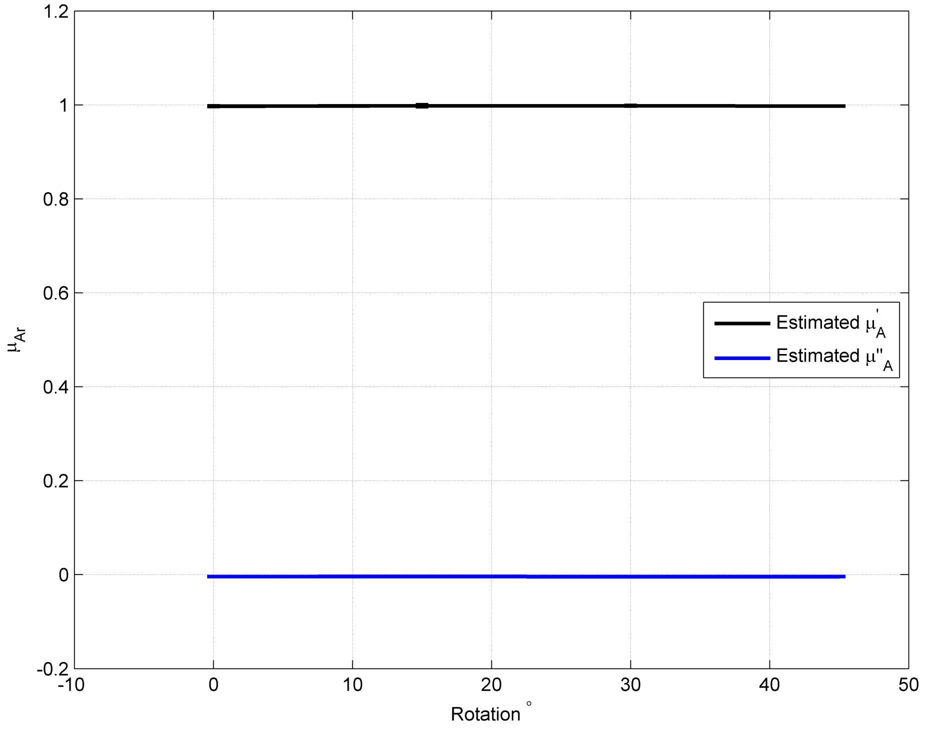

Figure 4.21: Complex permeability along A axis compared to rotation.

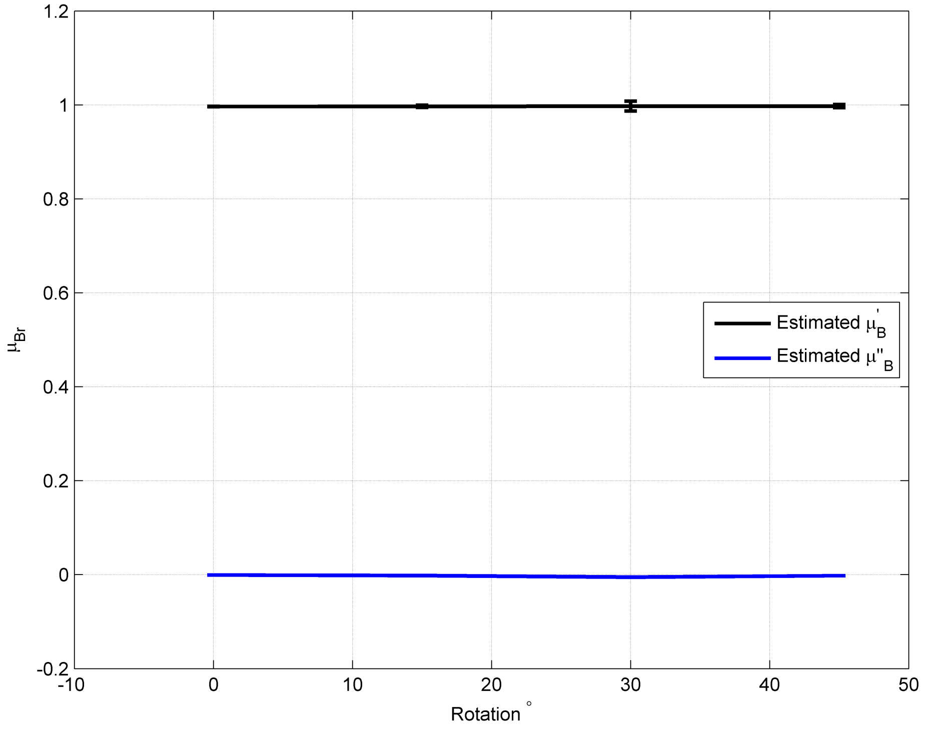

Figure 4.22: Complex permeability along B axis compared to rotation.

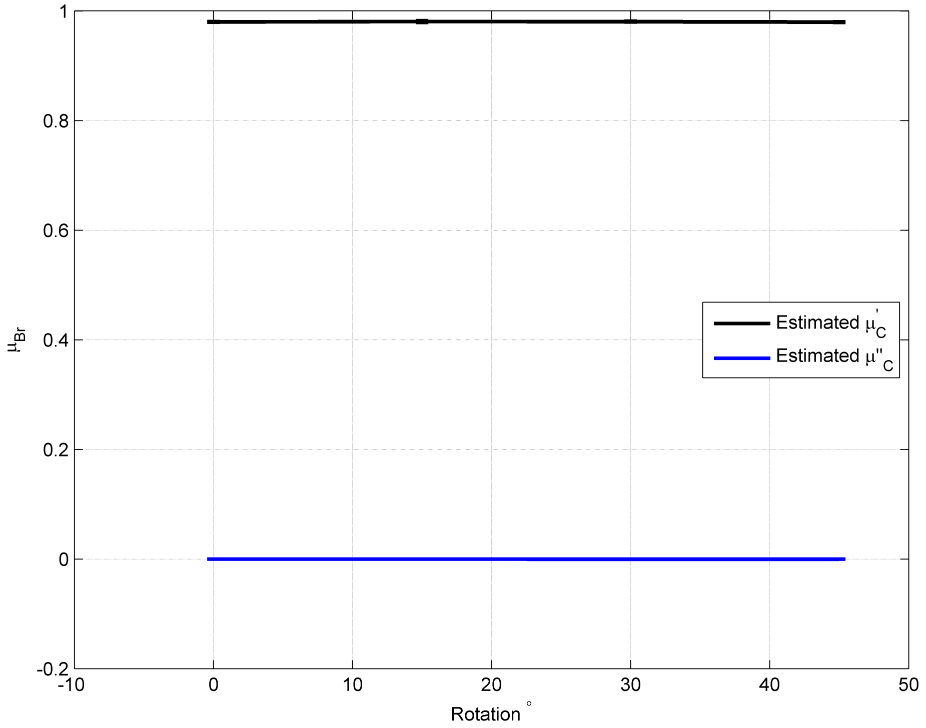

Figure 4.23: Complex permeability along C axis compared to rotation.

4.4 Summary of Results

The results shown in Chapter 4 show that the primary factor for adjusting the permittivity of a material by introduction of air vias is the ratio of air-to-dielectric. In this research project the vias ranged from 1 to 5 mm upon each dimension meaning they are electrically small compared to the excitation wavelength of 3.75 to 2.5 cm. Due to this fact the configuration of the vias showed almost no noticeable affect on the permeability. This can be seen by the testing of multiple different configurations of vias with the same air-to-dielectric ratio yielding the same permittivity. The trend of the material properties was easily mappable to a simple cubic function dependent solely on the air-to-dielectric ratio for the case of symmetric vias. Also, the if a non-lossy bulk material was used the material remained non-lossy after introduction of the air vias. The permeability of the material was unchanged by the introduction of the vias assuming that the material was non-magnetic. Rotation of the vias also tended to have almost no effect on the final permittivity and permeability of the final metamaterial allowing for some small variation in manufacturing without altering the material properties.

Future Research

Suggested future progress for this research progress would be to collaborate with Dr. Havrilla et. al. to have some designed samples machined and characterized by the measurement process outlined in [8]. This process would provide an outside verification for the design parameters outlined in this research project. Also, developing a statistical analysis as to how the ratio between the A and B dimensions of the vias can effect the corresponding electromagnetic properties. A study of the contrast between the dielectric values of the base material and air would provide insight into the relations of power and energy. Finally, further analysis of how non-square vias can be used to effect the electromagnetic properties.

Bibliography

[1] Smith, David. ”Electromagnetic Metamaterials.” David R. Smith Group. N.p., n.d. Web. 24 Oct. 2014.

[2] Kundtz, N. Advances in complex artificial electromagnetic media. Diss. PhD Dissertation, Duke University, Durham, N. Carolina, 2009.

[3] Popa, Bogdan-Ioan, Jeffery Allen, and Steven A. Cummer. ”Conformal array design with transformation electromagnetics.” Applied Physics Letters 94.24 (2009): 244102.

[4] Pendry, John B., David Schurig, and David R. Smith. ”Controlling electromagnetic fields.” science 312.5781 (2006): 1780-1782.

[5] M. A. Saville, Notes parameter estimation biaxial material, unpublished.

[6] Balanis, Constantine A. Advanced engineering electromagnetics. Vol. 20. New York: Wiley, 1989.

[7] Schey, H. M. Div, Grad, Curl, and All That; an Informal Text on Vector Calculus. New York: Norton, 1973. Print.

[8] A. Knisely, ”Biaxial Anisotropic Material Characterization using Rectangular to Square Waveguide,” in *Antenna Measurement Techniques Association.*, Tucson, AZ, 2014

[9] B. R. Crowgey, et al., Characterization of Biaxial Anisotropic Material Using a Reduced Aperture Waveguide, IEEE Transactions on Instrumentation and Measurement, vol. 62, no. 10, pp. 2739-2750, October 2013.

[10] B. R. Crowgey, Rectangular Waveguide Material Characterization: Anisotropic Property Extraction and Measurement Validation, PhD Dissertation, Michigan State University, 2013.

[11] Jin, Jianming. The finite element method in electromagnetics. John Wiley Sons, 2014.

[12] Chew, Weng Cho. Waves and fields in inhomogeneous media. Vol. 522. New York: IEEE press, 1995.

[13] Akhtar, M. Jaleel, Lambert E. Feher, and Manfred Thumm. ”A waveguide-based two-step approach for measuring complex permittivity tensor of uniaxial composite materials.” Microwave Theory and Techniques, IEEE Transactions on 54.5 (2006): 2011-2022.

[14] Yin, HongCheng, ZengMing Chao, and YanPing Xu. ”A new freespace method for measurement of electromagnetic parameters of biaxial materials at microwave frequencies.” Microwave and Optical Technology Letters 46.1 (2005): 72-78.

[15] Morin, Gilbert, and Manfred Nachman. ”A new method for measuring anisotropy at microwave frequencies.” Instrumentation and Measurement, IEEE Transactions on 28.3 (1979): 198-204.

[16] Nicolson, A. M., and G. F. Ross. ”Measurement of the intrinsic properties of materials by time-domain techniques.” Instrumentation and Measurement, IEEE Transactions on 19.4 (1970): 377-382.